



# Numerical Heat Transfer, Part A: Applications

## An International Journal of Computation and Methodology

ISSN: (Print) (Online) Journal homepage: <https://www.tandfonline.com/loi/unht20>

# Simplified PN finite element approximations for coupled natural convection and radiation heat transfer

Jaafar Albadr, Mofdi El-Amrani & Mohammed Seaid

To cite this article: Jaafar Albadr, Mofdi El-Amrani & Mohammed Seaid (2023) Simplified PN finite element approximations for coupled natural convection and radiation heat transfer, Numerical Heat Transfer, Part A: Applications, 83:5, 478-502, DOI: [10.1080/10407782.2022.2091897](https://doi.org/10.1080/10407782.2022.2091897)

To link to this article: <https://doi.org/10.1080/10407782.2022.2091897>



© 2022 The Author(s). Published with license by Taylor & Francis Group, LLC



Published online: 05 Jul 2022.



Submit your article to this journal [↗](#)



Article views: 694



View related articles [↗](#)



View Crossmark data [↗](#)



Citing articles: 1 View citing articles [↗](#)

# Simplified $P_N$ finite element approximations for coupled natural convection and radiation heat transfer

Jaafar Albadr<sup>a</sup>, Mofdi El-Amrani<sup>b</sup>, and Mohammed Seaid<sup>a</sup>

<sup>a</sup>Department of Engineering, University of Durham, England, UK; <sup>b</sup>Dpto. Matemáticas Aplicada, Universidad Rey Juan Carlos, Móstoles, Madrid, Spain

## ABSTRACT

This article focuses on the effect of radiative heat on natural convection heat transfer in a square domain inclined with an angle. The left vertical wall of the enclosure is heated while maintaining the vertical right wall at room temperature with both adiabatic upper and lower horizontal walls. The governing equations are Navier–Stokes equations subjected to Boussinesq approximation to account the change in density. The natural convection–radiation equations are solved continuously to obtain the temperature, velocity and pressure. Taylor–Hood finite element approach has been adopted to solve the equations using triangular mesh. Effects of Rayleigh number, Planck constant and optical depth on the results are considered, presented and analyzed. Results show that the adiabatic walls, Planck constant as well as the inclined angle play an important role in the distribution of heat transfer inside the cavity.

## ARTICLE HISTORY

Received 28 January 2022

Accepted 25 May 2022

## KEYWORDS

Characteristic-Galerkin method; natural convection–radiation; radiative transfer; simplified  $P_N$  approximations

## 1. Introduction

Natural convection–radiation heat transfer problems can be found in many industrial and realistic applications such as building insulations, double glazed windows and solar collectors. Among the past work, in [1] numerical calculations have been done for obtaining results for a square cavity at Rayleigh numbers between  $10^3$  and  $10^6$  as a benchmark solution. Finite volume method (FVM) has been adopted to solve Navier–Stokes equations and discrete ordinates methods (DOM) has been accounted for the radiative transfer equations (RTE). Results showed that different values of Rayleigh number (Ra) and optical thickness  $\tau$  affect on the transfer of heat across the cavity. However, the study was limited to a fixed Planck constant (Pl) of 0.1 without considering the effect of the inclined angle. In [2], natural convection–radiation interaction has been studied a square enclosure at different values of Pl,  $\tau$  and Ra. RTE has been solved utilizing five different approaches, DOM, FVM,  $P_1$ ,  $SP_3$  and  $P_3$ . Nevertheless, the study was limited as the effect of the inclined angle has not been considered. Furthermore, in [3] numerical investigation has been conducted for natural thermal flow under laminar and turbulent conditions inside a square cavity using the control volume method with Ra up to  $10^{10}$ . Nonetheless, only convection heat has been investigated to solve the conservation equations. Likewise, in [4] a combined heat transfer of radiation and natural convection study has been investigated in a square cavity containing participating gases. The effect of Ra of values between  $10^3$  and  $10^6$  with  $\tau$  values from 0 to 100 on temperature, velocity

**CONTACT** Jaafar Albadr  [jnalbader@yahoo.com](mailto:jnalbader@yahoo.com)  Department of Engineering, University of Durham, South Road, Durham, England, DH1 3LE, UK.

© 2022 The Author(s). Published with license by Taylor & Francis Group, LLC

This is an Open Access article distributed under the terms of the Creative Commons Attribution-NonCommercial-NoDerivatives License (<http://creativecommons.org/licenses/by-nc-nd/4.0/>), which permits non-commercial re-use, distribution, and reproduction in any medium, provided the original work is properly cited, and is not altered, transformed, or built upon in any way.

distribution and Nusselt numbers have been studied. The study on the other hand was limited to convection heat transfer and cannot be used for complex geometries as finite difference method (FDM) has been used. Moreover, in [5, 6]  $P_1$  approximation for representing the radiative heat transfer has been utilized in narrow vertical cavities. The effect of radiation on the transition, conduction and boundary condition has been dealt with. However, the study was limited to  $P_1$  approximation without the effect of the inclined angle. Additionally, [7, 8] investigated the interaction between natural convection and radiation with and without participating media for an undivided cavity with wide range of Ra and Pl. However, in [7] FDM has been considered which cannot be used for complex geometries and in [8], the effect of optical depth and the inclined angle have not been presented. In [9], radiation–natural convection heat transfer has been investigated in an inclined rectangular enclosure at different Rayleigh numbers and inclined angles using FVM for solving the governing equations. It has been found a reduction in the effect of heat transfer when the increase in the inclined angle was considered. The study however didn't consider the effect of Pl or the  $\tau$ . In [10], an absorbing, emitting and isotropically scattering medium at three different Ra and a wide range of radiation–conduction parameters have been studied inside a square enclosure using nonlinear successive–over–relaxation method for combining radiation and convection–conduction heat transfer. Yet, the effect of the inclined angle, Pl and  $\tau$  have not been taken into account. In [11], interaction effect between convection and radiation has been taken into account in a square cavity with inclined angle. The method used is FDM which is limited to simple geometries. Results showed the heat transfer were affected by the inclined angle, emissivity and Ra. The result was limited to a constant  $\tau$  of unity and Pl of 0.1. Furthermore, in [12], a numerical study has been considered for the effect of radiation–convection heat transfer in a slanted cavity with two different angles of  $45^\circ$  and  $60^\circ$ . FVM has been considered with different ranges of  $\tau$ . The study was limited to one value of Ra at a fixed Pl. Moreover, in [13], convection radiation heat transfer has been investigated experimentally and numerically. The numerical investigation has been done using finite volume CFD code ANSYS Fluent. The study has been considered variety values of Ra and inclined angle. Results showed that the maximum heat rate was at an inclined angle of 0. The limitations in this study were regulating the effect of radiation as the commercial software can deal with radiation transfer equations properly. In addition, in [14], a numerical investigation has been carried out based on thermosolute buoyancies with Soret and Dufour effects for double-diffusive convection. The model has been discretized using FVM and solved utilizing SIMPLE algorithm with QUICK scheme in nonuniform staggered mesh. Heat transfer characteristics has been investigated with different values of Ra, Soret and Dufour coefficients, aspect ratios and buoyancy ratios. The average Sherwood as well as Nusselt numbers was kept constant without considering the radiation effect or the inclined angle. what is more, in [15], a numerical analysis of combined double diffusion radiation convection transfer of heat in a square cavity has been conducted using FDM and DOM for the RTE. Results showed that heat transfer was affected by  $\tau$ . However, the study used FDM which can only be used for simple geometries and the effect of Pl and the inclined angle were not investigated. Furthermore, in [16], a convection–radiation transfer of heat has been accounted for a rotating cavity of a square shape with a local heater. The nondimensional mathematical formulation has been solved by FDM. The influence of Ra, Nusselt number, Taylor number, emissivity and Ostrogradsky number on the natural heat flow has been studied. The results showed that the increase in the emissivity as well as the rotation reduce the temperature inside the heating element. Notwithstanding, the study cannot be applied to complex geometries due to the limitations of FDM. Likewise, in [17], a double-diffusive natural convection study for Soret and Dufour effects as well as viscosity dissipation in a square cavity filled with Bingham fluid has been simulated by FD Lattice Boltzmann technique. Various values of Ra, Lewis number, Bingham number, Echart number, Dufour and Soret parameters, Buoyancy ratio and inclined angle has been carried out. Results showed that mass transfer increases with the increase in Soret parameter while the heat transfer increases with the increase in Dufour parameter for different values of Ra and Bingham

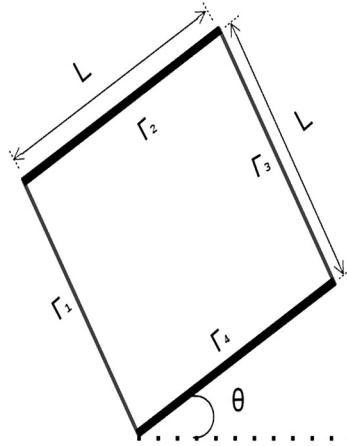


**Figure 1.** The geometry of the squared cavity used in the current study.

numbers. The rise in both Dufour and Soret parameters enhances the raises the fluid friction and enhances the generation of entropy. Results also showed that the growing in the buoyancy ration boosts heat and mass transfer. The augmentation of Eckret number decreases the transfer of heat while the increase in Ra number decreases the average Bejan number. From another point of view, the study cannot be used for considering complex geometries and it misses the effect of radiation heat transfer. A thorough investigation of the numerical performance of the  $SP_N$  hierarchy in the context of coupled radiation, convection and diffusion problems are given. We examine the accuracy and efficiency of the  $SP_N$  approximations of radiative transfer for natural convection problems in a square enclosure with the effect of the inclined angle. The vertical walls of the enclosure are heated with uniform different temperatures and the horizontal walls are adiabatic. A Boussinesq approximation of the Navier–Stokes equations is employed for the fluid subject to combined natural convection and radiation. Coupled with the  $SP_N$  models, the system of equations results into a set of partial differential equations independent of the angle variable and easy to be numerically solved using standard computational fluid dynamics methods. We believe that this is the first investigation on the effect of convection–radiation heat transfer using Taylor Hood finite element method with  $SP_3$  approximations. Previous studies failed to show a noticeable difference between radiation and pure convection. This is due to the fact that previous researchers focused on considering the  $P_1$  radiative equations which are discussed in this article. Furthermore, to the best of our knowledge another novelty lies in the complex geometry heater that is added to the square cavity with two different inclined angles.

The article is organized as follows. In [Section 2](#) Geometric set up and an introduction to the coupled system consisting of the Boussinesq approximation and the radiative transfer equation will be presented. The .. approximations are formulated in [Section 3](#), where we will especially introduce the  $SP_0$ ,  $SP_1$  and the  $SP_3$  systems. The numerical methods for the solution of these coupled systems are based on a characteristic-Galerkin method which is presented in [Section 4](#). [Section 5](#) shows the validation for the code. Finally, numerical results are discussed in [Section 6](#), where we compare the different models for different flow and radiation regimes. Especially, we present numerical comparisons for a wide range of physical parameters, e.g. the optical depth, the Prandtl number, the Planck constant and the Rayleigh number. Conclusions are given in [Section 7](#).

## 2. Equations for natural convection–radiation

A schematic of the system considered in the present work is shown in [Figure 1](#). The system consists of a squared enclosure with sides of length  $L$  and inclination angle  $\theta'$  subject to a thermal

variation  $(T'_H - T'_C)$ , where  $T'_H$  and  $T'_C$  are temperatures of the hot and cold boundary walls. Here and in what follows, primed variables refer to dimensional quantities. The enclosure consists of a gray, absorbing, emitting and nonscattering fluid surrounded by rigid black walls. The fluid is Newtonian and all the thermo-physical properties are assumed to be constant, except for density in the buoyancy term that can be adequately modeled by the Boussinesq approximation while compression effects and viscous dissipation are neglected [18]. With these assumptions, the governing equations consist of:

Conservation of mass:

$$\frac{\partial u'}{\partial x} + \frac{\partial v'}{\partial y} = 0. \quad (2.1)$$

Conservation of  $x$ -momentum:

$$\frac{\partial u'}{\partial t} + u' \frac{\partial u'}{\partial x} + v' \frac{\partial u'}{\partial y} + \frac{1}{\rho} \frac{\partial p'}{\partial x} = \nu \left( \frac{\partial^2 u'}{\partial x^2} + \frac{\partial^2 u'}{\partial y^2} \right) + g\beta(T' - T_\infty) \sin \theta'. \quad (2.2)$$

Conservation of  $y$ -momentum:

$$\frac{\partial v'}{\partial t} + u' \frac{\partial v'}{\partial x} + v' \frac{\partial v'}{\partial y} + \frac{1}{\rho} \frac{\partial p'}{\partial y} = \nu \left( \frac{\partial^2 v'}{\partial x^2} + \frac{\partial^2 v'}{\partial y^2} \right) + g\beta(T' - T_\infty) \cos \theta'. \quad (2.3)$$

Conservation of energy:

$$\rho_\infty c_p \left( \frac{\partial T'}{\partial t} + u' \frac{\partial T'}{\partial x} + v' \frac{\partial T'}{\partial y} \right) = \lambda \left( \frac{\partial^2 T'}{\partial x^2} + \frac{\partial^2 T'}{\partial y^2} \right) - \nabla \cdot \mathbf{Q}'_R. \quad (2.4)$$

where  $T_\infty$  is the reference temperature,  $\rho_\infty$  the reference density,  $\mathbf{u}' = (u', v')^T$  the velocity field,  $p'$  the pressure,  $T'$  the temperature,  $\nu$  the kinematic viscosity,  $c_p$  the specific heat at constant pressure,  $g$  the gravity constant,  $\beta$  the coefficient of thermal expansion, and  $\lambda$  the thermal conductivity. The effect of radiation is taken into consideration in the energy equation as the divergence of radiative heat flux,  $\nabla \cdot \mathbf{Q}'_R$ . For a gray medium, this term is given by

$$-\nabla \cdot \mathbf{Q}'_R = \int_{\mathbb{S}^2} \kappa(B'(T') - I') d\omega, \quad (2.5)$$

where  $I' = I'(\omega, \mathbf{x})$  is the spectral intensity at position  $\mathbf{x} = (x, y)^T$  and propagating along the angular direction  $\omega$  in the unit sphere  $\mathbb{S}^2$ . For a nonscattering medium, the intensity  $I'$  is obtained from the radiative transfer equation

$$\omega \cdot \nabla I' + \kappa I' = \kappa B'(T'), \quad (2.6)$$

where  $\kappa$  is the absorption coefficient and  $B'(T)$  is the spectral intensity of the black-body radiation given by the Planck function [19].

$$B'(T) = \sigma_B T^4, \quad (2.7)$$

with  $\sigma_B$  is the Boltzmann constant. Since it is convenient to work with dimensionless formulations, we define the following nondimensional variables

$$\alpha = \frac{\lambda}{\rho c_p}, \quad \mathbf{x} = \frac{\mathbf{x}'}{L}, \quad t = \frac{\alpha t'}{L^2}, \quad \mathbf{u} = \frac{L \mathbf{u}'}{\alpha}, \quad p = \frac{p' L^2}{\rho_\infty \alpha^2}, \quad T = \frac{T' - T'_C}{T'_H - T'_C},$$

$$\kappa = \frac{\kappa'}{\kappa_\infty}, \quad I = \frac{I'}{\sigma_B T_\infty^4}, \quad Q_R = \frac{Q'_R}{\sigma_B T_\infty^4}, \quad \theta = \frac{\theta'}{\theta_\infty}, \quad j = \frac{T'_H - T'_C}{T_\infty}.$$

where  $\alpha$  is thermal diffusivity,  $j$  is a general parameter used in the calculation of the non-dimensional radiation energy. We also define the optical depth  $\tau$ , the Prandtl number  $Pr$ , the Rayleigh number  $Ra$ , and the Planck constant  $Pl$ , as

$$\tau = \kappa_{\text{ref}}L, \quad Pr = \frac{\nu}{\alpha}, \quad Ra = \frac{\beta g(T'_H - T'_C)L^3}{\nu\alpha}, \quad Pl = \frac{j\lambda}{\sigma_B T_\infty^2 L}. \quad (2.8)$$

Hence, Equations (2.1)–(2.4) can be rewritten in dimensionless form as

$$\begin{aligned} \nabla \cdot \mathbf{u} &= 0, \\ \frac{D\mathbf{u}}{Dt} + \nabla p - Pr\nabla^2\mathbf{u} &= RaPrT\mathbf{e}, \\ \frac{DT}{Dt} - \nabla^2 T &= -\frac{1}{Pl}\nabla \cdot \mathbf{Q}_R, \end{aligned} \quad (2.9)$$

where  $\mathbf{e} = (\sin\theta, \cos\theta)^T$  is the unit vector associated with the inclination angle and  $\frac{Dw}{Dt}$  is the material derivative of any physical variable  $w$  defined by

$$\frac{Dw}{Dt} = \frac{\partial w}{\partial t} + \mathbf{u} \cdot \nabla w. \quad (2.10)$$

The dimensionless radiative heat flux is given by

$$\nabla \cdot \mathbf{Q}_R = \frac{1}{\tau}(\varphi - B(T)), \quad (2.11)$$

where  $\varphi$  is the total incident radiation defined as

$$\varphi(\mathbf{x}) = \int_{\mathbb{S}^2} I(\omega, \mathbf{x}) d\omega. \quad (2.12)$$

The scaled Planck function is given by

$$B(T) = 4T^4.$$

The radiative transfer equation (2.6) can be rewritten in a dimensionless as

$$\tau\omega \cdot \nabla I + \kappa I = \kappa B(T). \quad (2.13)$$

To formulate a well-posed problem, Equations (2.9) and (2.13) have to be solved in a bounded domain  $\Omega$  with a smooth boundary  $\partial\Omega$  and subject to given initial and boundary conditions. As shown in Figure 1:

$$\partial\Omega = \Gamma_1 \cup \Gamma_2 \cup \Gamma_3 \cup \Gamma_4, \quad (2.14)$$

where  $\Gamma_1$  and  $\Gamma_3$  represent the hot and cold walls, respectively, whereas  $\Gamma_2$  and  $\Gamma_4$  are adiabatic walls. Hence, the boundary conditions are

$$\mathbf{u}(t, \hat{\mathbf{x}}) = 0, \quad \forall \hat{\mathbf{x}} \in \partial\Omega, \quad (2.15)$$

for the flow, and

$$\begin{aligned} T(t, \hat{\mathbf{x}}) &= T_H, & \forall \hat{\mathbf{x}} \in \Gamma_1, \\ T(t, \hat{\mathbf{x}}) &= T_C, & \forall \hat{\mathbf{x}} \in \Gamma_3, \\ \mathbf{n}(\hat{\mathbf{x}}) \cdot \nabla T(t, \hat{\mathbf{x}}) &= 0, & \forall \hat{\mathbf{x}} \in \Gamma_2 \cup \Gamma_4, \end{aligned} \quad (2.16)$$

for the temperature. In (2.16),  $\mathbf{n}(\hat{\mathbf{x}})$  denotes the outward unit normal in  $\hat{\mathbf{x}}$  with respect to  $\partial\Omega$ . For the radiative transfer, the boundary conditions are for diffuse black walls

$$\begin{aligned}
 I(\hat{\mathbf{x}}, \omega) &= B(T_H), & \forall \hat{\mathbf{x}} \in \Gamma_1^-, \\
 I(\hat{\mathbf{x}}, \omega) &= B(T_C), & \forall \hat{\mathbf{x}} \in \Gamma_3^-, \\
 \mathbf{n}(\hat{\mathbf{x}}) \cdot \nabla I(t, \hat{\mathbf{x}}) &= 0, & \forall \hat{\mathbf{x}} \in \Gamma_2^- \cup \Gamma_4^-,
 \end{aligned} \tag{2.17}$$

where the boundary regions  $\Gamma_i^-$  are defined as

$$\Gamma_i^- = \{ \hat{\mathbf{x}} \in \Gamma_i : \mathbf{n}(\hat{\mathbf{x}}) \cdot \omega < 0 \}, \quad i = 1, \dots, 4.$$

### 3. Simplified $P_N$ equations

It is evident that the coupled problem presented in Section 2 is numerically involved due to the directional dependence of the radiative intensity. A major reduction of the discrete phase space can be achieved, if one replaces the radiative transfer equation by a new model which only involves physical quantities independent of the angular direction. One possibility to do so is the usage of the so-called simplified  $P_N$  approximations [19]. For the sake of completeness, we briefly formulate the asymptotic analysis of the radiative transfer equation. The starting point is to rewrite equation (2.13) as

$$\left( 1 + \frac{\tau}{\kappa} \omega \cdot \nabla \right) I = B(T).$$

Then, we apply a Neumann series to formally invert the transport operator

$$\begin{aligned}
 I &= \left( 1 + \frac{\tau}{\kappa} \omega \cdot \nabla \right)^{-1} B(T), \\
 &\approx \left( 1 - \frac{\tau}{\kappa} \omega \cdot \nabla + \frac{\tau^2}{\kappa^2} (\omega \cdot \nabla)^2 - \frac{\tau^3}{\kappa^3} (\omega \cdot \nabla)^3 + \dots \right) B(T).
 \end{aligned}$$

Integrating respect to  $\omega$  over all directions in the unit sphere  $\mathbb{S}^2$  and using

$$\int_{\mathbb{S}^2} (\omega \cdot \nabla)^n d\omega = (1 + (-1)^n) \frac{2\pi}{n+1} \nabla^n,$$

we obtain the formal asymptotic equation for  $\varphi$

$$4\pi B(T) = \left( 1 - \frac{\tau^2}{3\kappa^2} \nabla^2 - \frac{4\tau^4}{45\kappa^4} \nabla^4 - \frac{44\tau^6}{945\kappa^6} \nabla^6 \right) \varphi + \mathcal{O}(\tau^8). \tag{3.1}$$

When terms of  $\mathcal{O}(\tau^2)$ ,  $\mathcal{O}(\tau^4)$ ,  $\mathcal{O}(\tau^6)$  or  $\mathcal{O}(\tau^8)$  are neglected, we obtain the  $SP_0$ ,  $SP_1$ ,  $SP_2$  or  $SP_3$  approximations, respectively. Higher order approximations can be derived in a similar manner.

The  $SP_0$  approximation reduces (3.1) to

$$\varphi = 4\pi B(T). \tag{3.2}$$

This corresponds to the thermodynamic equilibrium for which the radiation effects are dropped out from the energy equation in (2.9). In the present work, we consider only the  $SP_1$  and  $SP_3$  approximations and our techniques can be straightforwardly extended to other  $SP_N$  approximations. Thus,

The  $SP_1$  approximation:

$$4\pi B(T) = \varphi - \frac{\tau^2}{3\kappa^2} \nabla^2 \varphi + \mathcal{O}(\tau^4),$$

which is equivalent to

$$-\frac{\tau^2}{3\kappa}\nabla^2\varphi + \kappa\varphi = 4\pi\kappa B(T). \tag{3.3}$$

The SP<sub>3</sub> approximation:

$$4\pi B(T) = \left(1 - \frac{\tau^2}{3\kappa}\nabla^2 - \frac{4\tau^4}{45\kappa^4}\nabla^4 - \frac{44\tau^6}{945\kappa^6}\nabla^6\right)\varphi + \mathcal{O}(\tau^8),$$

and its associated equations are given by

$$\begin{aligned} -\frac{\tau^2}{\kappa}\mu_1^2\nabla^2\varphi_1 + \kappa\varphi_1 &= 4\pi\kappa B(T), \\ -\frac{\tau^2}{\kappa}\mu_2^2\nabla^2\varphi_2 + \kappa\varphi_2 &= 4\pi\kappa B(T). \end{aligned} \tag{3.4}$$

The new variables  $\varphi_1$  and  $\varphi_2$  in (3.4) are related to the total incident intensity (2.12) by

$$\varphi = \frac{\gamma_2\varphi_1 - \gamma_1\varphi_2}{\gamma_2 - \gamma_1}. \tag{3.5}$$

Once the mean intensity  $\varphi$  is obtained from the above SP<sub>N</sub> approximations the radiative heat flux is formulated as in (2.11). The boundary conditions for SP<sub>N</sub> approximations are derived from variational principles and are strongly connected to the P<sub>N</sub> approximations Marshak’s conditions, compare [19]. Here, we formulate boundary conditions for the SP<sub>N</sub> approximations which are consistent with temperature boundary conditions (2.16). For more general formulation of these boundary conditions and further details are there in [20]. Hence, the boundary conditions for the SP<sub>1</sub> equation (3.3) are

$$\begin{aligned} \frac{\tau}{3\kappa}\mathbf{n}(\hat{\mathbf{x}}) \cdot \nabla\varphi(t, \hat{\mathbf{x}}) + \varphi(t, \hat{\mathbf{x}}) &= B(T_H), & \forall \hat{\mathbf{x}} \in \Gamma_1, \\ \frac{\tau}{3\kappa}\mathbf{n}(\hat{\mathbf{x}}) \cdot \nabla\varphi(t, \hat{\mathbf{x}}) + \varphi(t, \hat{\mathbf{x}}) &= B(T_C), & \forall \hat{\mathbf{x}} \in \Gamma_3, \\ \mathbf{n}(\hat{\mathbf{x}}) \cdot \nabla\varphi(t, \hat{\mathbf{x}}) &= 0, & \forall \hat{\mathbf{x}} \in \Gamma_2 \cup \Gamma_4. \end{aligned} \tag{3.6}$$

For the SP<sub>3</sub> equations (3.4), boundary conditions are given by

$$\begin{aligned} \frac{\tau}{\kappa}\mathbf{n}(\hat{\mathbf{x}}) \cdot \nabla\varphi_1(t, \hat{\mathbf{x}}) + \alpha_1\varphi_1(t, \hat{\mathbf{x}}) &= \eta_1B(T_H) + \beta_2\varphi_2(t, \hat{\mathbf{x}}), & \forall \hat{\mathbf{x}} \in \Gamma_1, \\ \frac{\tau}{\kappa}\mathbf{n}(\hat{\mathbf{x}}) \cdot \nabla\varphi_1(t, \hat{\mathbf{x}}) + \alpha_1\varphi_1(t, \hat{\mathbf{x}}) &= \eta_1B(T_C) + \beta_2\varphi_2(t, \hat{\mathbf{x}}), & \forall \hat{\mathbf{x}} \in \Gamma_3, \\ \frac{\tau}{\kappa}\mathbf{n}(\hat{\mathbf{x}}) \cdot \nabla\varphi_2(t, \hat{\mathbf{x}}) + \alpha_2\varphi_2(t, \hat{\mathbf{x}}) &= \eta_2B(T_H) + \beta_1\varphi_1(t, \hat{\mathbf{x}}), & \forall \hat{\mathbf{x}} \in \Gamma_1, \\ \frac{\tau}{\kappa}\mathbf{n}(\hat{\mathbf{x}}) \cdot \nabla\varphi_2(t, \hat{\mathbf{x}}) + \alpha_2\varphi_2(t, \hat{\mathbf{x}}) &= \eta_2B(T_C) + \beta_1\varphi_1(t, \hat{\mathbf{x}}), & \forall \hat{\mathbf{x}} \in \Gamma_3, \\ \mathbf{n}(\hat{\mathbf{x}}) \cdot \nabla\varphi_1(t, \hat{\mathbf{x}}) = \mathbf{n}(\hat{\mathbf{x}}) \cdot \nabla\varphi_2(t, \hat{\mathbf{x}}) &= 0, & \forall \hat{\mathbf{x}} \in \Gamma_2 \cup \Gamma_4. \end{aligned} \tag{3.7}$$

It is noteworthy that these parameters are valid only when nonreflective boundary conditions are supplied to the radiative transfer equation (2.13). In [20], mathematical formulae to handle more general boundary conditions in (2.13) are provided.

### 4. Numerical solution procedure

Since standard Galerkin discretization leads to the central difference approximation of differential operators, Galerkin approximations to the convection equations usually suffer instability problems. Among various techniques to improve stability, streamline upwind Petrov–Galerkin, Taylor–Galerkin and characteristic–Galerkin schemes have gained some popularity. The characteristic–Galerkin scheme discretizes the original equation in time along the characteristic curves

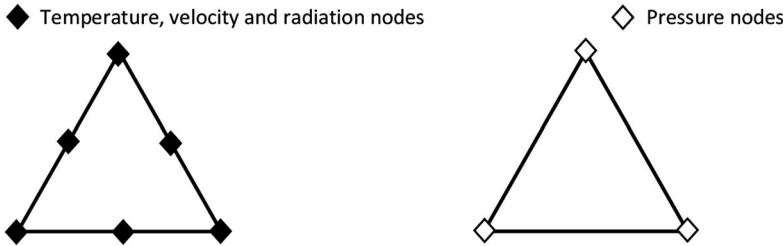


**Figure 2.** Definition of Taylor–Hood finite element.

before applying the spatial discretization. It can be implemented in the framework of standard Galerkin finite element formulation. In this section we briefly describe the ingredients of the numerical scheme used and for more details we refer to [21–24] and further references are cited therein.

Let us choose a time step  $\Delta t$  and discretize the time domain into subintervals  $[t_n, t_{n+1}]$  with  $t_n = n\Delta t$  and  $n = 0, 1, \dots$ . For any generic function  $w$  we denote  $w^n(\mathbf{x}) = w(\mathbf{x}, t_n)$ , we also denote by  $\mathbf{X}(\mathbf{x}, t_{n+1}; t)$  the characteristic curves associated with the material derivative (2.10) which solve the following initial value problem

$$\begin{aligned} \frac{d\mathbf{X}(\mathbf{x}, t_{n+1}; t)}{dt} &= \mathbf{u}(\mathbf{X}(\mathbf{x}, t_{n+1}; t), t), \quad \forall (\mathbf{x}, t) \in \bar{\Omega} \times [t_n, t_{n+1}], \\ \mathbf{X}(\mathbf{x}, t_{n+1}; t_{n+1}) &= \mathbf{x}. \end{aligned} \quad (4.1)$$

Notice that  $\mathbf{X}(\mathbf{x}, t_{n+1}; t) = (X(\mathbf{x}, t_{n+1}; t), Y(\mathbf{x}, t_{n+1}; t))^T$  is the departure point and represents the position at time  $t$  of a particle that reaches the point  $\mathbf{x} = (x, y)^T$  at time  $t_{n+1}$ . Hence, for all  $\mathbf{x} \in \bar{\Omega} = \Omega \cup \partial\Omega$  and  $t \in [t_n, t_{n+1}]$  the solution of (4.1) can be expressed as

$$\mathbf{X}(\mathbf{x}, t_{n+1}; t_n) = \mathbf{x} - \int_{t_n}^{t_{n+1}} \mathbf{u}(\mathbf{X}(\mathbf{x}, t_{n+1}; t), t) dt. \quad (4.2)$$

Accurate estimation of the characteristic curves  $\mathbf{X}(\mathbf{x}, t_{n+1}; t_n)$  is crucial to the overall accuracy of the characteristic-Galerkin method. In this article, we used a method first proposed in [25] in the context of semi-Lagrangian schemes to integrate the weather prediction equations. Details on formulation and implementation of this step for characteristics-based methods can be found in references [21, 26, 27] and are not repeated here.

The discretization of the space domain  $\bar{\Omega}$  is proceed as follows. Given  $h_0$ ,  $0 < h_0 < 1$ , let  $h$  be a spatial discretization parameter such that  $0 < h < h_0$ . We generate a quasi-uniform partition  $\Omega_h \subset \bar{\Omega}$  of small elements  $\mathcal{T}_j$  that satisfy the following conditions:

- i.  $\bar{\Omega} = \cup_{j=1}^{Ne} \mathcal{T}_j$ , where  $Ne$  is the number of elements of  $\Omega_h$ .
- ii. If  $\mathcal{T}_i$  and  $\mathcal{T}_j$  are two different elements of  $\Omega_h$ , then

$$\mathcal{T}_i \cap \mathcal{T}_j = \begin{cases} P_{ij}, & \text{a mesh point, or} \\ \Gamma_{ij}, & \text{a common side, or} \\ \emptyset, & \text{emptyset.} \end{cases}$$

- iii. There exists a positive constant  $k$  such that for all  $j \in \{1, \dots, Ne\}$ ,  $\frac{d_j}{h_j} > k$  ( $h_j \leq h$ ), where  $d_j$  is the diameter of the circle inscribed in  $\mathcal{T}_j$  and  $h_j$  is the largest side of  $\mathcal{T}_j$ .

The conforming finite element spaces for velocity–temperature–radiation and pressure that we use are Taylor–Hood finite elements  $P_m/P_{m-1}$  i.e., polynomial of degree  $m \geq 2$  for  $\{u, v, T, \varphi\}$  and polynomial of degree  $m - 1$  for  $\{p\}$  on simplices, respectively. An illustration is depicted in

Figure 2 for triangular mesh. It is known that for such elements the discrete velocity–temperature–radiation and pressure fields satisfy the inf-sup condition. This property guarantees the stability and convergence of the approximate solutions, compare [28, 29]. These elements can be defined as

$$V_h = \left\{ v_h \in C^0(\bar{\Omega}) : v_h|_{T_j} \in S(T_j), \quad \forall T_j \in \Omega_h \right\},$$

$$Q_h = \left\{ q_h \in C^0(\bar{\Omega}) : q_h|_{T_j} \in R(T_j), \quad \forall T_j \in \Omega_h \right\},$$

where  $C^0(\bar{\Omega})$  denotes the space of continuous and bounded functions in  $\bar{\Omega}$ ,  $S(T_j)$  and  $R(T_j)$  are polynomial spaces defined in  $T_j$  as  $S(K_j) = P_m(T_j)$  for simplices,  $S(T_j) = Q_m(T_j)$  for quadrilaterals,  $R(T_j) = P_{m-1}(T_j)$  for simplices and  $R(T_j) = Q_{m-1}(T_j)$  for quadrilaterals. Hence, we formulate the finite element solutions to  $u^n(\mathbf{x})$ ,  $v^n(\mathbf{x})$ ,  $T^n(\mathbf{x})$ ,  $\varphi^n(\mathbf{x})$  and  $p^n(\mathbf{x})$  as

$$u_h^n = \sum_{j=1}^M U_j^n \phi_j, \quad v_h^n = \sum_{j=1}^M V_j^n \phi_j, \quad T_h^n = \sum_{j=1}^M \Lambda_j^n \phi_j,$$

$$\varphi_h^n = \sum_{j=1}^M \xi_j^n \phi_j, \quad p_h^n = \sum_{j=1}^N P_j^n \psi_j,$$
(4.3)

where  $M$  and  $N$  are respectively, the number of velocity–temperature–radiation and pressure mesh points in the partition  $\Omega_h$ . The functions  $U_j^n$ ,  $V_j^n$ ,  $\Lambda_j^n$  and  $P_j^n$  are the corresponding nodal values of  $u_h^n(\mathbf{x})$ ,  $v_h^n(\mathbf{x})$ ,  $T_h^n(\mathbf{x})$  and  $p_h^n(\mathbf{x})$ , respectively. They are defined as  $U_j^n = u_h^n(\mathbf{x}_j)$ ,  $V_j^n = v_h^n(\mathbf{x}_j)$ ,  $\Lambda_j^n = T_h^n(\mathbf{x}_j)$  and  $P_j^n = p_h^n(\mathbf{y}_j)$  where  $\{\mathbf{x}_j\}_{j=1}^M$  and  $\{\mathbf{y}_j\}_{j=1}^N$  are the set of velocity–temperature–radiation and pressure mesh points in the partition  $\Omega_h$ , respectively, so that  $N < M$  and  $\{\mathbf{y}_1, \dots, \mathbf{y}_N\} \subset \{\mathbf{x}_1, \dots, \mathbf{x}_M\}$ . In (4.3),  $\{\phi_j\}_{j=1}^M$  and  $\{\psi_j\}_{j=1}^N$  are the set of global nodal basis functions of  $V_h$  and  $S_h$ , respectively, characterized by the property  $\phi_i(\mathbf{x}_j) = \delta_{ij}$  and  $\psi_i(\mathbf{y}_j) = \delta_{ij}$  with  $\delta_{ij}$  denoting the Kronecker symbol.

Assuming that, for all  $j = 1, \dots, M$ , the pairs  $(\mathbf{X}_{hj}^n, \hat{T}_j)$  and the mesh point values  $\{U_j^n, V_j^n, \Lambda_j^n\}$  are known, we compute the values  $\{\hat{U}_j^n, \hat{V}_j^n, \hat{\Lambda}_j^n\}$  as

$$\hat{U}_j^n := u_h^n(\mathbf{X}_{hj}^n) = \sum_{k=1}^M U_k \phi_k(\mathbf{X}_{hj}^n), \quad \hat{V}_j^n := v_h^n(\mathbf{X}_{hj}^n) = \sum_{k=1}^M V_k \phi_k(\mathbf{X}_{hj}^n),$$

$$\hat{\Lambda}_j^n := T_h^n(\mathbf{X}_{hj}^n) = \sum_{k=1}^M \Lambda_k \phi_k(\mathbf{X}_{hj}^n).$$
(4.4)

Then, the solution  $\{\hat{u}_h^n(\mathbf{x}), \hat{v}_h^n(\mathbf{x}), \hat{T}_h^n(\mathbf{x})\}$  at the characteristic feet is obtained by

$$\hat{u}_h^n(\mathbf{x}) = \sum_{j=1}^M \hat{U}_j^n \phi_j(\mathbf{x}), \quad \hat{v}_h^n(\mathbf{x}) = \sum_{j=1}^M \hat{V}_j^n \phi_j(\mathbf{x}), \quad \hat{T}_h^n(\mathbf{x}) = \sum_{j=1}^M \hat{\Lambda}_j^n \phi_j(\mathbf{x}).$$
(4.5)

We should mention that the conventional characteristic-Galerkin methods in [22, 23] evaluate  $\hat{u}_h^n$ ,  $\hat{v}_h^n$  and  $\hat{T}_h^n$  using an  $L^2$ -projection on the space of the velocity–temperature–radiation  $V_h$ . In many applications, the evaluation of integrals in the  $L^2$ -projection is difficult and computationally very demanding.

The procedure to advance the solution of (2.9) and (3.3) or (2.9) and (3.4) from a time  $t_n$  to the next time  $t_{n+1}$  can be carried out in the following steps:

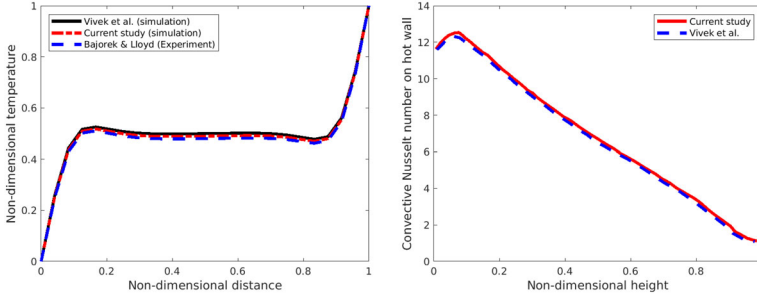


**Figure 3.** A comparison for the cross-sectional of the dimensionless temperature with Bajorek and Lloyd [31] and Vivek et al. [11] (left) and the convective Nusselt number (right) at  $Ra = 3.557 \times 10^5$ .

1. Solve for  $\varphi^{n+1}$

$$-\frac{\tau^2}{3\kappa} \nabla^2 \varphi^{n+1} + \kappa \varphi^{n+1} = \kappa B(\hat{T}^n), \quad (4.6)$$

subject to the boundary conditions (3.6) in case of  $SP_1$  approximation or

$$-\frac{\tau^2}{\kappa} \mu_1^2 \nabla^2 \varphi_1^{n+1} + \kappa \varphi_1^{n+1} = \kappa B(\hat{T}^n), \quad (4.7)$$

$$-\frac{\tau^2}{\kappa} \mu_2^2 \nabla^2 \varphi_2^{n+1} + \kappa \varphi_2^{n+1} = \kappa B(\hat{T}^n), \quad (4.8)$$

$$\varphi^{n+1} = \frac{\gamma_2 \varphi_1^{n+1} - \gamma_1 \varphi_2^{n+1}}{\gamma_2 - \gamma_1}.$$

subject to the boundary conditions (3.7) in case of the  $SP_3$  approximation.

2. Solve for  $T^{n+1}$

$$\frac{T^{n+1} - \hat{T}^n}{\Delta t} - \nabla^2 T^{n+1/2} = -\frac{1}{jPl} \nabla \cdot \mathbf{Q}_R^{n+1}, \quad (4.9)$$

subject to the boundary conditions (2.16).

3. Solve for  $\bar{\mathbf{u}}^{n+1}$

$$\frac{\bar{\mathbf{u}}^{n+1} - \hat{\mathbf{u}}^n}{\Delta t} + \gamma \nabla p^n - Pr \nabla^2 \bar{\mathbf{u}}^{n+1/2} = Ra Pr T^{n+1/2} \mathbf{e}, \quad \text{in } \Omega, \quad (4.10)$$

$$\bar{\mathbf{u}}^{n+1} = \mathbf{0}, \quad \text{on } \Gamma.$$

4. Solve for  $\bar{p}$  and  $\mathbf{u}^{n+1}$

$$\frac{\mathbf{u}^{n+1} - \bar{\mathbf{u}}^{n+1}}{\Delta t} + \nabla \bar{p} = \mathbf{0}, \quad \text{in } \Omega, \quad (4.11)$$

$$\nabla \cdot \mathbf{u}^{n+1} = 0, \quad \text{in } \Omega,$$

$$\mathbf{n} \cdot \nabla \mathbf{u}^{n+1} = 0, \quad \text{on } \Gamma.$$

5. Update  $p^{n+1}$

$$p^{n+1} = p^n + 2\bar{p}.$$

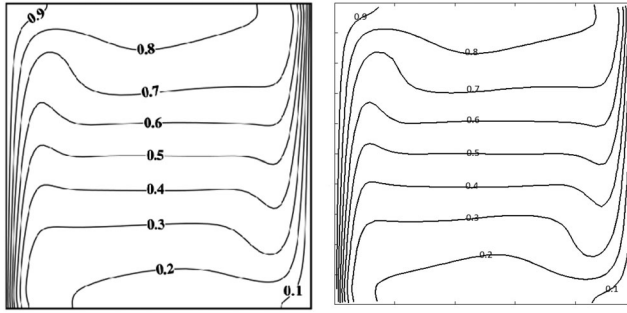


Figure 4. A comparison for the temperature contours for the current study (right) and the results obtained by [1] at  $Ra = 10^6$ .

In (4.9) and (4.10),  $T^{n+1/2}$  and  $\bar{\mathbf{u}}^{n+1/2}$  are defined as

$$T^{n+1/2} = \frac{1}{2}T^{n+1} + \frac{1}{2}\hat{T}^n, \quad \bar{\mathbf{u}}^{n+1/2} = \frac{1}{2}\bar{\mathbf{u}}^{n+1} + \frac{1}{2}\hat{\mathbf{u}}^n,$$

Note that, the solution of (4.11) leads to a pressure-Poisson problem for  $\bar{p}$  of the form

$$\begin{aligned} \nabla^2 \bar{p} &= \frac{1}{\Delta t} \nabla \cdot \bar{\mathbf{u}}^{n+1}, & \text{in } \Omega, \\ \mathbf{n} \cdot \nabla \bar{p} &= 0, & \text{on } \Gamma. \end{aligned} \tag{4.12}$$

Notice that, the integration of equations (4.6)–(4.12) for triangular elements is easy and described in many text books, compare [30] among others. Furthermore, in the solution procedure, four linear systems have to be solved at each time step to update the solution  $\{p^{n+1}, u^{n+1}, v^{n+1}, T^{n+1}, \varphi^{n+1}\}$  from (4.6) to (4.12). To solve these linear systems in our method we have implemented a preconditioned conjugate gradient algorithm

### 5. Code validation

The results have been extensively checked on benchmark problems to check the accuracy. For verification of the numerical results, we have compared our results with different published cases. The first validation that has been considered is comparing the accuracy of our code with the experimental results obtained by Bajorek and Lloyd [31] for the pure heat convection an air-filled vertical squared cavity with all surfaces coated in black. The right and left sides were the hot and cold walls, while the bottom and top are maintained adiabatic. The results also have been validated with the simulation results obtained by Vivek et al. [11] for the convection heat transfer for the temperature values at the mid-height of the domain. Figure 3 shows an excellent agreement to the horizontal cross-sectional study for the dimensionless temperature at the middle of the square cavity along with the Nusselt number validation on the hot wall with [11] at  $Ra = 3.557 \times 10^5$ ,  $T_H = 312.1$  K,  $T_C = 296.6$  K. The next validation that has been considered is comparing our results with the results obtained by [1] for pure convection. The upper and lower sides of the cavity remained adiabatic, while heat transferred from the hot wall located on the left to the cold wall which in on the right. Figure 4 shows a very good agreement with our results obtained from the temperature contour at  $Ra = 10^6$ . The third validation has been accounted for the pure double diffusion for a squared enclosure. The right and left walls have been set as hot and cold sources respectively with no heat transfer from the upper and lower walls. Figure 5 shows the isotherms results which show an agreement between the current study and the study that has been done by [15] and [17] at  $Ra = 10^4$ . The fourth Validation that has been investigated by comparing our results with the results taken by [17] for double diffusion at  $Ra = 10^5$ . Figure 6 shows the agreement with our current study results for the temperature distribution across the square

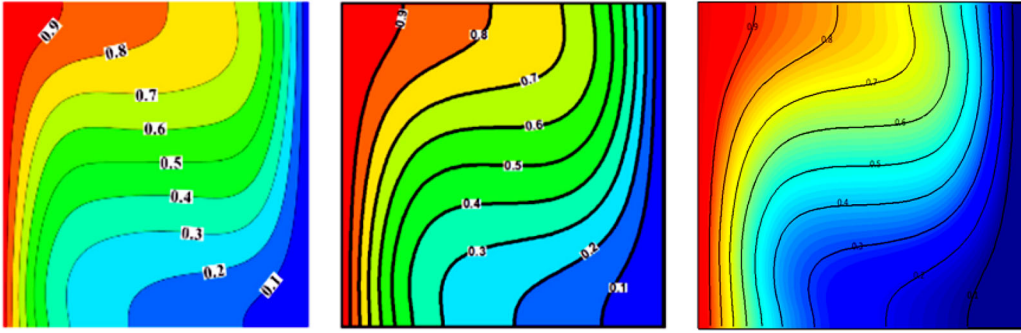


**Figure 5.** A comparison for the temperature contour for the current study (right) and the results obtained by [15] (left) and the results done by [17] (middle) at  $Ra = 10^4$ .

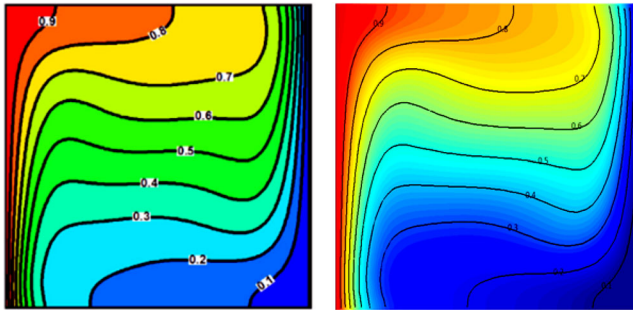


**Figure 6.** A comparison for the temperature contours for the current study (right) and the results obtained by [17] at  $Ra = 10^5$  (left).

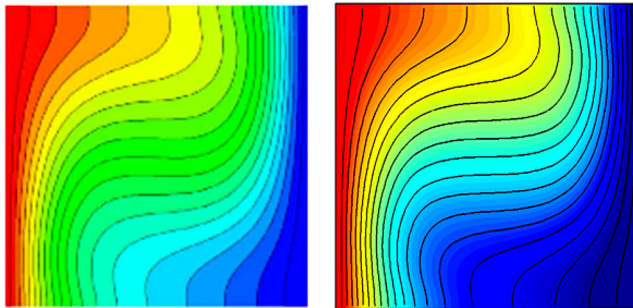


**Figure 7.** A comparison for the temperature contours for the current study (right) and the results obtained by [2] at  $Ra = 10^4$ ,  $Pl = 1.0$ ,  $\tau = 5$  (left).

cavity with the same set of walls than have been adopted by the previous references. The fifth validation examined is with the inclusion of the radiation transfer of heat in a squared cavity. [Figure 7](#) shows the comparison that has been obtained with the results recorded by [2] for accounting radiation at  $Ra = 10^4$ ,  $Pl = 1.0$ ,  $\tau = 5$ . It is worth mentioning that our approach is valid for low values of  $\tau$ . In [2], it was reported that at high values of  $\tau$ , convective heat became dominant and there was no effect for the radiation. We have performed the same exact values of the pertinent parameters for calculating only the heat convection. Our results matches the results conducted by [2] and shown in [Figure 7](#). Our final validation that has been accounted for the effect of radiation–convection. The current results have been compared with cross-sectional results examined by [1] at  $Ra = 10^4$  and  $10^5$  with a fixed  $\tau$  of 1 and  $Pl = 0.1$ . [Figure 8](#) shows a very good agreement with our results taken for the horizontal cross-sectional study for the temperature at the

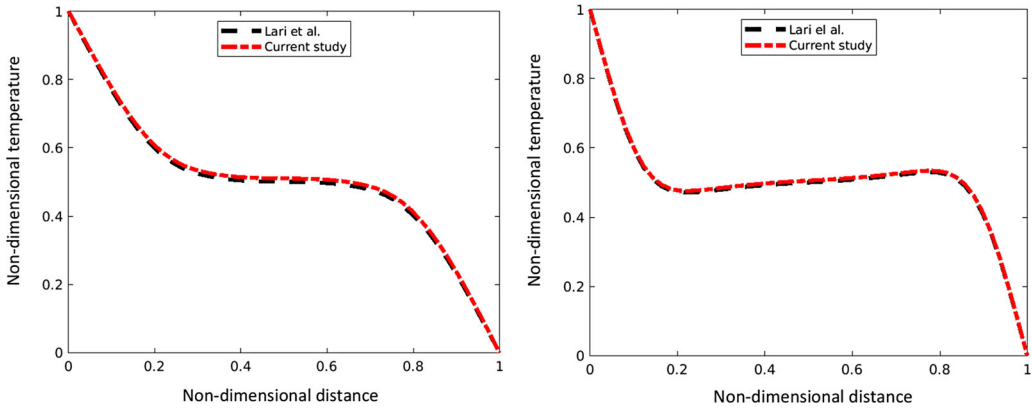


**Figure 8.** A comparison for the cross-sectional nondimensional temperature along the nondimensional  $x$  axis in the middle of the square cavity obtained by [1] and the current study at  $Ra = 10^4$  (left) and  $Ra = 10^5$  (right) at  $Pr = 0.1$  and  $\tau = 1$ .

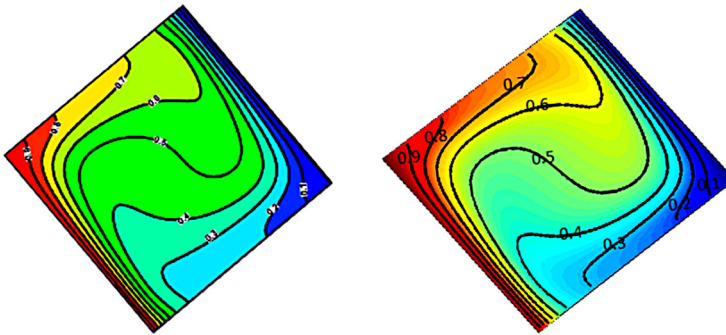


**Figure 9.** A comparison between the convection results from current study (right) and the results obtained by [17] (left) for an angle of  $40^\circ$  and with  $Ra = 10^5$ .

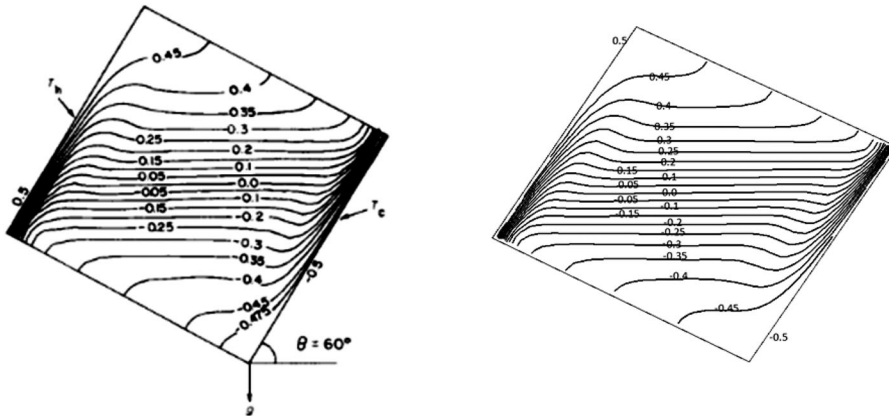


**Figure 10.** A comparison between the convection results from current study (right column) and the results obtained by [32] (left column) for an angle of  $40^\circ$  (upper row) and an angle of  $120^\circ$  (lower row) with  $Ra = 10^6$ .

middle of the enclosure. The second part of the validation is taking into account the inclined angle as well as the circular heater inside the cavity. Figure 9 show an excellent match with the results obtained by [17] at an angle value of  $40^\circ$  and with  $Ra = 10^5$  the inclined left and right walls are the hot and cold walls respectively, while maintaining adiabatic inclined top and bottom

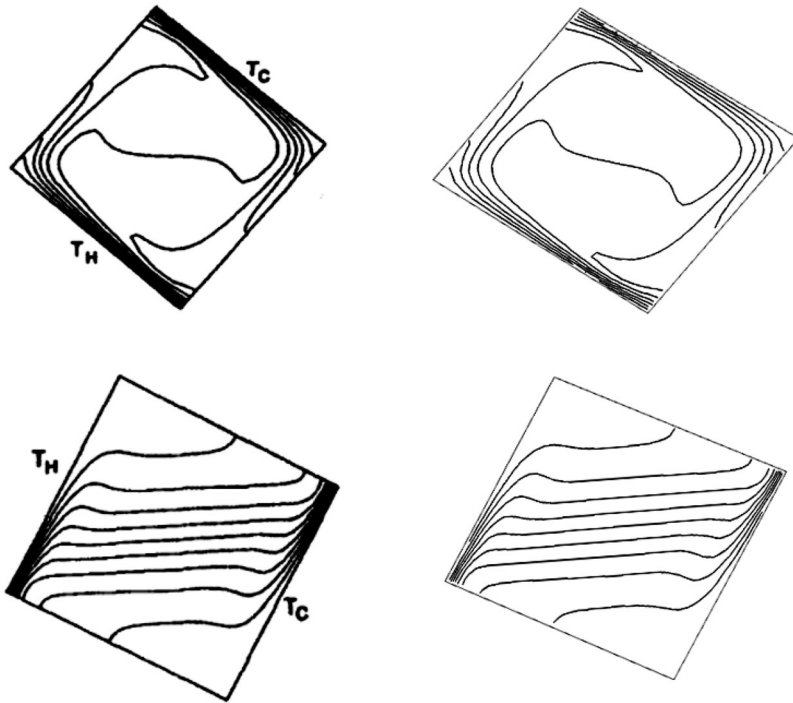


**Figure 11.** A comparison between the convection results from current study (right) and the results obtained by [33] (left) for an angle of  $60^\circ$  with  $Ra = 10^6$ .

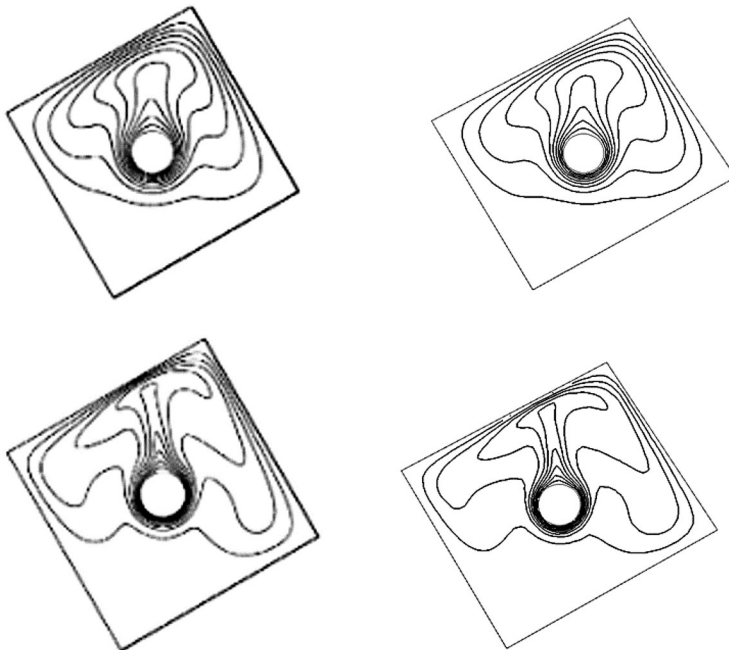


**Figure 12.** A comparison between the convection results from current study (right column) and the results obtained by [34] (left column) for an angle of  $30^\circ$  for  $Ra = 10^5$  (upper row) and  $Ra = 10^6$  lower row with a circular heater diameter of 0.1.

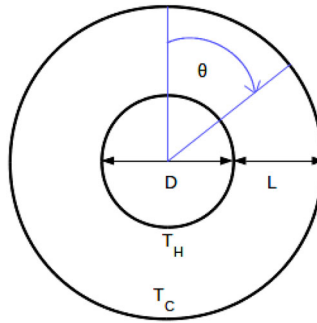


Figure 13. Cross-sectional view of the annulus geometry with  $\theta$  is the angle that moves in a clockwise direction.

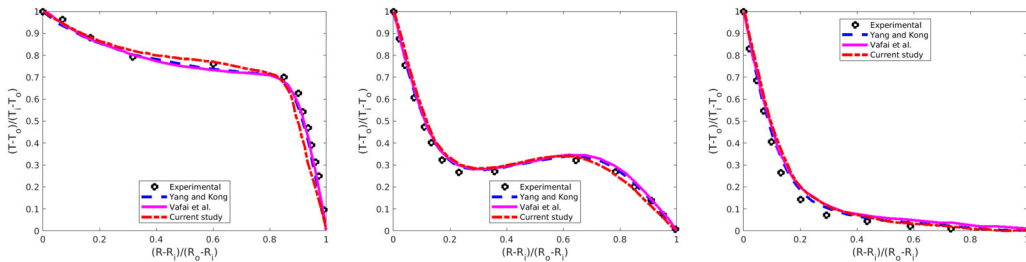


Figure 14. Comparison between our work and the published results from Kuehn and Goldstein [35], numerical data from Yang and Kong [36] and simulation study from Vafai et al. [37] at an angle of  $0^\circ$  (left),  $90^\circ$  (middle) and an angle of  $180^\circ$  (right) for values of  $Ra = 5 \times 10^5$  and  $Pr = 0.7$ .

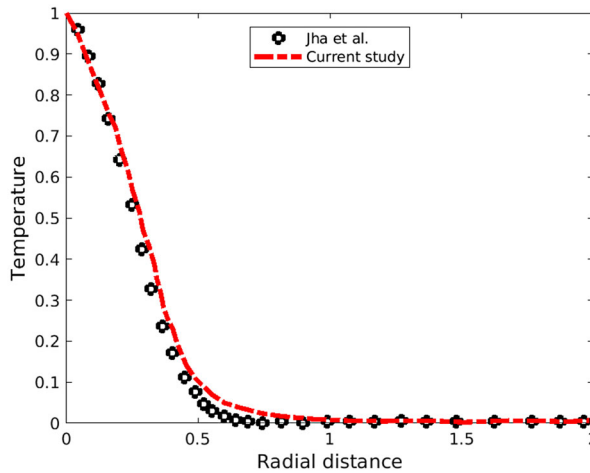
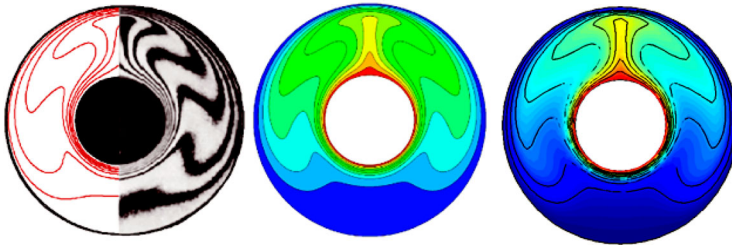
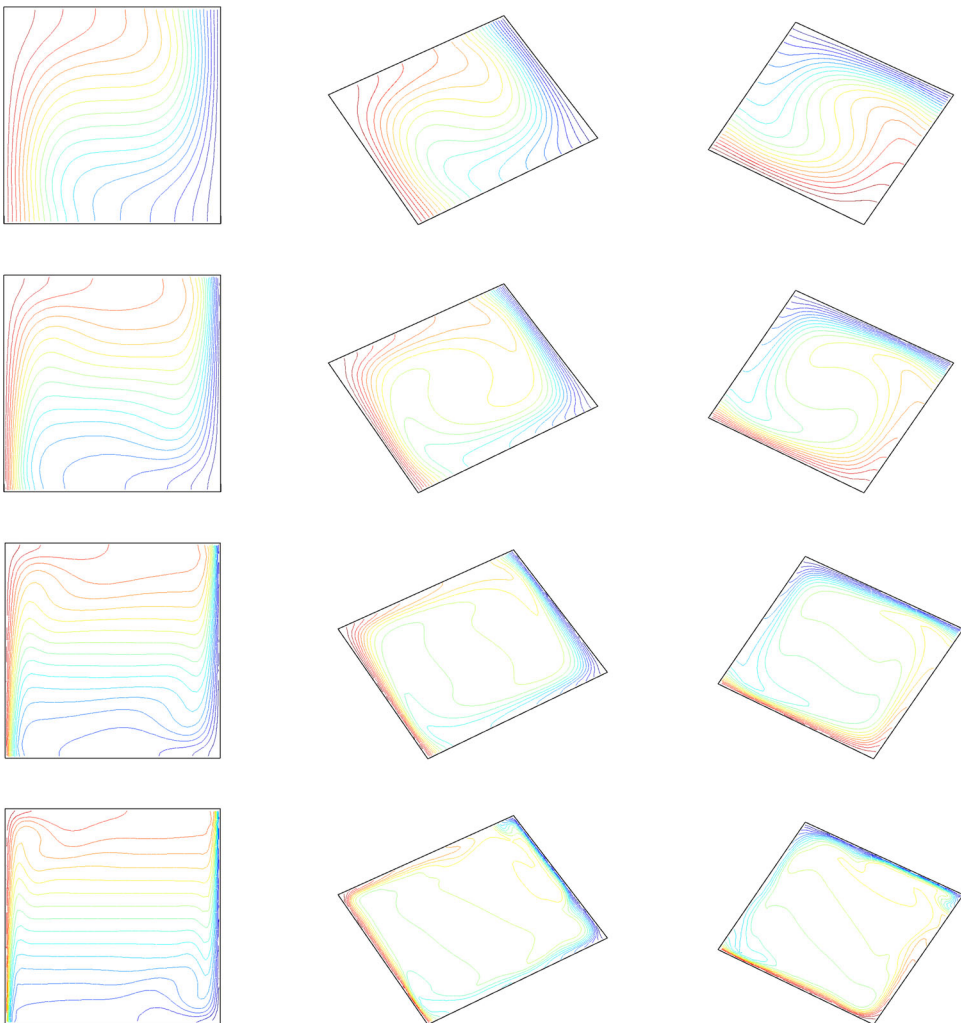


Figure 15. Comparison of convection–radiation results between the current study and the published work by Jha et al. [38] for  $Pr = 7$ , temperature difference parameter  $C_T=1.5$ , and perturbation parameter  $R=0.1$ .

walls. Another validation that has been accounted for with the results from two inclined angles of  $40^\circ$  and  $120^\circ$  obtained by [32] with  $Ra = 10^6$ . Figure 10 shows a very good match with our convective heat results. Another validation is also taken into consideration by comparing our results with the results measure by [33] for a square enclosure with an inclined angle of  $60^\circ$  with  $Ra = 10^6$ . Figure 11 shows a close results compared with our conducted results. The final validation



**Figure 16.** Comparison of temperature plume between the current study (right) and the published simulation work by Sheikholeslami et al. [39] (the left part of the left figure), interferograms from the experiment by Kuehn and Goldstein [35] (right part of the left figure) and simulation by Yang and Kong [36] (middle) for  $Pr = 0.706$  and  $Ra = 4.7 \times 10^4$ .



**Figure 17.** Temperature contour for the  $SP_3$  solution at  $Ra = 10^4$  (first row),  $Ra = 10^5$  (second row),  $Ra = 10^6$  (third row), and  $Ra = 10^7$  (fourth row) with  $Pr = 0.5$  at  $\theta = 0^\circ$  (first column),  $\theta = 30^\circ$  (second column) and  $\theta = 60^\circ$  (third column).

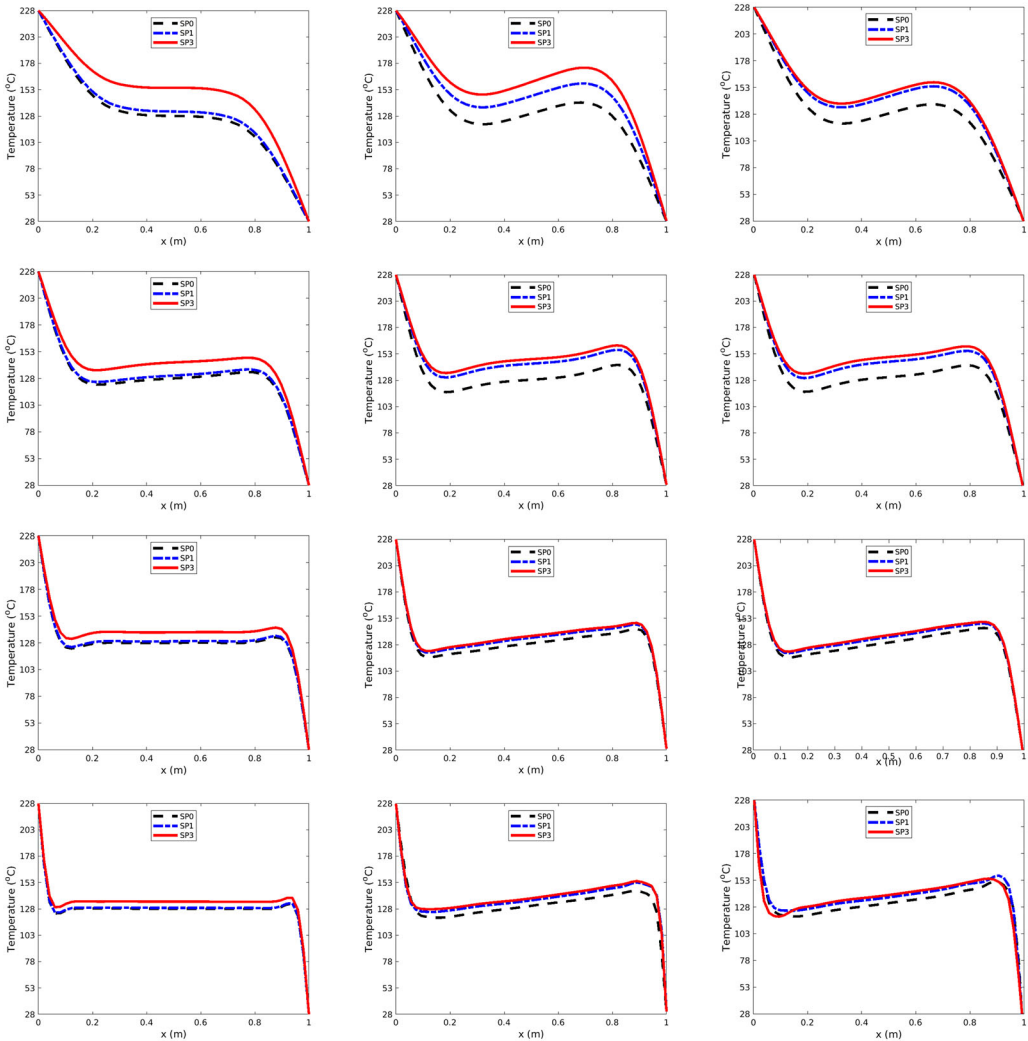


**Figure 18.** Temperature cross-sectional study for the pure convection  $SP_0$  and radiation–convection  $SP_1$  and  $SP_3$  solutions at  $Ra = 10^4$  (first row),  $Ra = 10^5$  (second row),  $Ra = 10^6$  (third row), and  $Ra = 10^7$  (fourth row) with  $PI = 0.2$  at  $\theta = 0^\circ$  (first column),  $\theta = 30^\circ$  (second column) and  $\theta = 60^\circ$  (third column).

considered is a cavity with inclined angle of  $30^\circ$  containing a circular heating source inside at two values of  $Ra$  of  $10^5$  and  $10^6$  with a circular heater diameter of 0.1. the inclined left and right walls are kept at cold temperatures while maintaining an inclined adiabatic upper and lower temperature. Figure 12 show the convection heat transfer results between the current results and the results done by [34].

### 5.7. Validation of convective–radiative heat transfer in a cylindrical annulus

Another validation that has been accounted for an annulus geometry shown in Figure 13. Figure 13 shows the diameter of the inner pipe of the heat exchanger.  $L$  is the space between the inner and the out pipes.  $T_H$  is the hot temperature,  $T_C$  is the cold temperature and  $\theta$  is the angle of rotation that moves in a clockwise direction. The value  $L/D$  has been considered according to the previous published work to match their dimensions. The first validation that

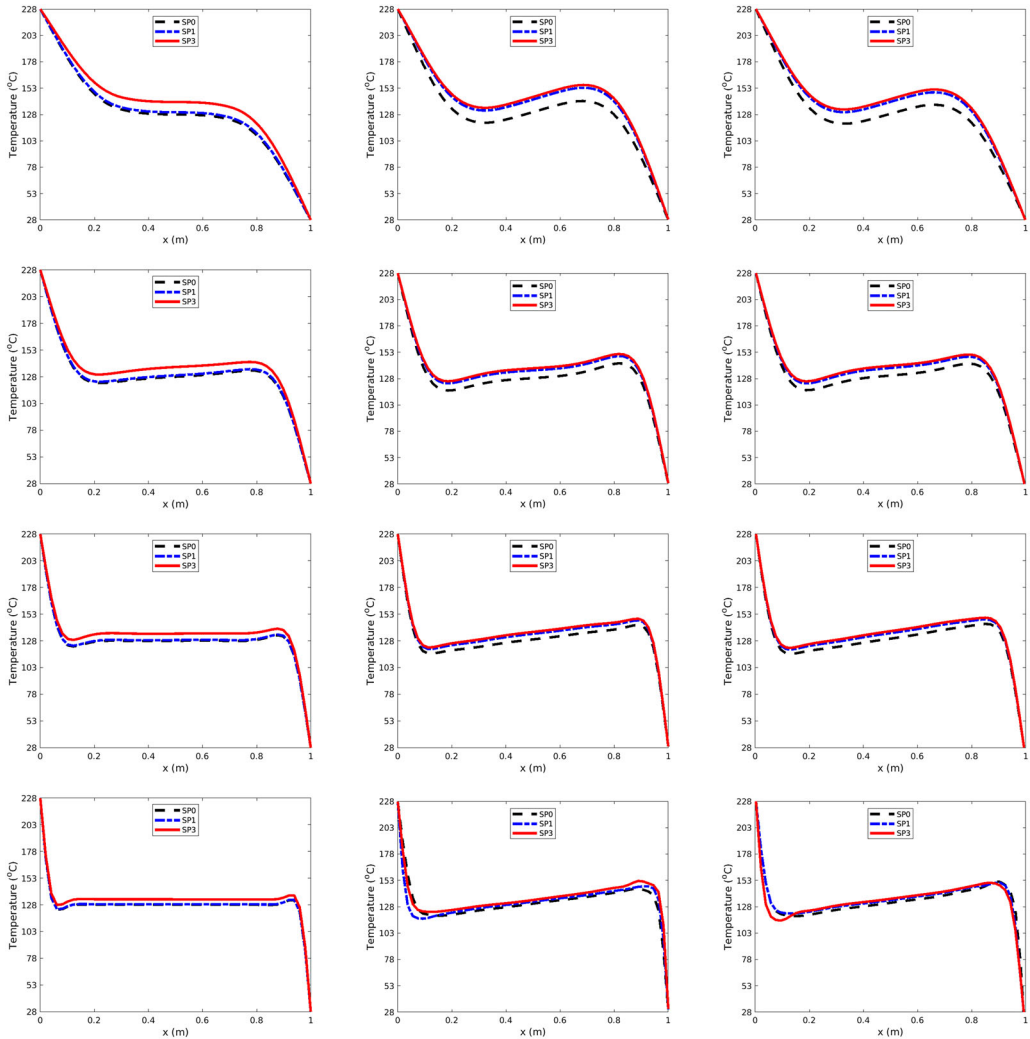


**Figure 19.** Temperature cross-sectional study for the pure convection  $SP_0$  and radiation-convection  $SP_1$  and  $SP_3$  solutions at  $Ra = 10^4$  (first row),  $Ra = 10^5$  (second row),  $Ra = 10^6$  (third row) and  $Ra = 10^7$  (fourth row) with  $PI = 0.5$  at  $\theta = 0^\circ$  (first column),  $\theta = 30^\circ$  (second column) and  $\theta = 60^\circ$  (third column).

has been considered in this study is a comparison of our convection heat transfer results with experimental data from [35], numerical data from [36] and numerical data from [37] at  $Ra = 5 \times 10^5$  and  $Pr = 0.7$  with three rotational angles of  $0^\circ$ ,  $90^\circ$  and  $180^\circ$ . Figure 14 shows a good match between the conducted results and the previous published data. The second validation that has been accounted for is the results conducted by Jha et al. [38] for the interaction of the natural convection heat with thermal radiation and our conducted results. Figure 15 illustrates an acceptable match of results between the current study and the published work by Jha et al. [38] for  $Pr = 7$ , temperature difference parameter  $C_T = 1.5$  and perturbation parameter  $R = 0.1$ . Another validation has been done by comparing the current study with the experimental results conducted by [35], simulation done by [39] and simulation accomplished by [36] for values of  $Ra = 4.7 \times 10^4$  and  $Pr = 0.706$ . It can be seen from Figure 16 that the temperature plume is in agreement with the mentioned results.

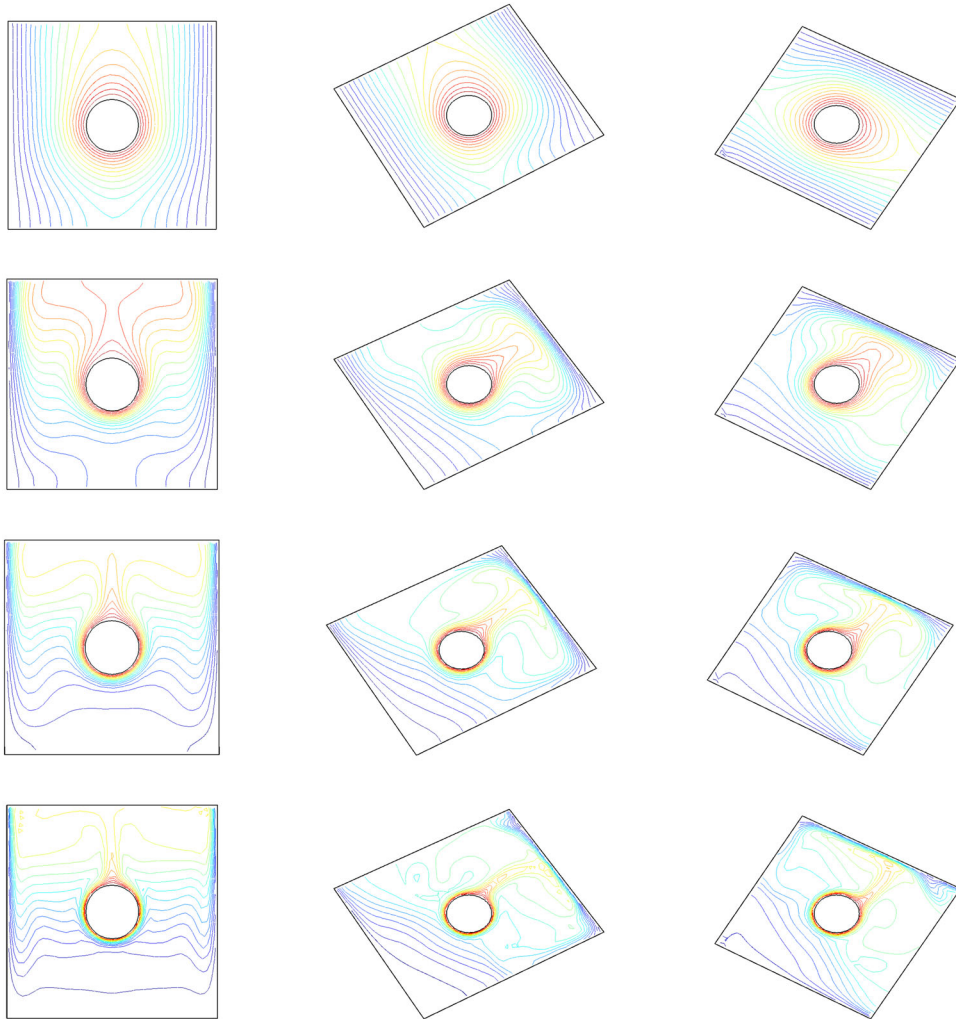


**Figure 20.** Temperature contour for the  $SP_3$  solution at  $Ra = 10^4$  (first row),  $Ra = 10^5$  (second row),  $Ra = 10^6$  (third row), and  $Ra = 10^7$  (fourth row) with  $Pl = 0.2$  at  $\theta = 0^\circ$  (first column),  $\theta = 30^\circ$  (second column) and  $\theta = 60^\circ$  (third column).

## 6. Numerical results

### 6.1. Square cavity without internal heater

In all the results presented hereinafter, certain variables are kept fixed using our own heat transfer characteristics and boundary conditions. The upper and the lower walls of the cavity are adiabatic. The hot wall on the left side is at temperature  $T_H = 228^\circ\text{C}$  while maintaining the temperature of the cold wall on the right side  $T_C = 28^\circ\text{C}$ . Prandtl number  $Pr = 0.707$  and  $\tau = 0.1$  (as fluid flows inside the cavity is considered air [40]). Different values of  $Ra$ ,  $Pl$ , the inclined angle  $\theta$  are considered to study the effect of temperature distribution over the cavity. The simulation experiments that are considered at  $Ra = 10^4 - 10^7$  with two different values of  $Pl = 0.2$  and  $0.5$  and three different angles  $\theta$  of  $0^\circ$ ,  $30^\circ$  and  $60^\circ$ . Figure 17 shows the temperature contour at a wide range of  $Ra$  with  $Pl = 0.5$  for  $SP_3$  approximations and for the considered angles. It can be seen that the circulation of flow inside the cavity is affected by the inclined angle. At  $\theta = 0^\circ$  and  $30^\circ$ , the flow circulates in a clockwise direction. However, at  $\theta = 60^\circ$ , the

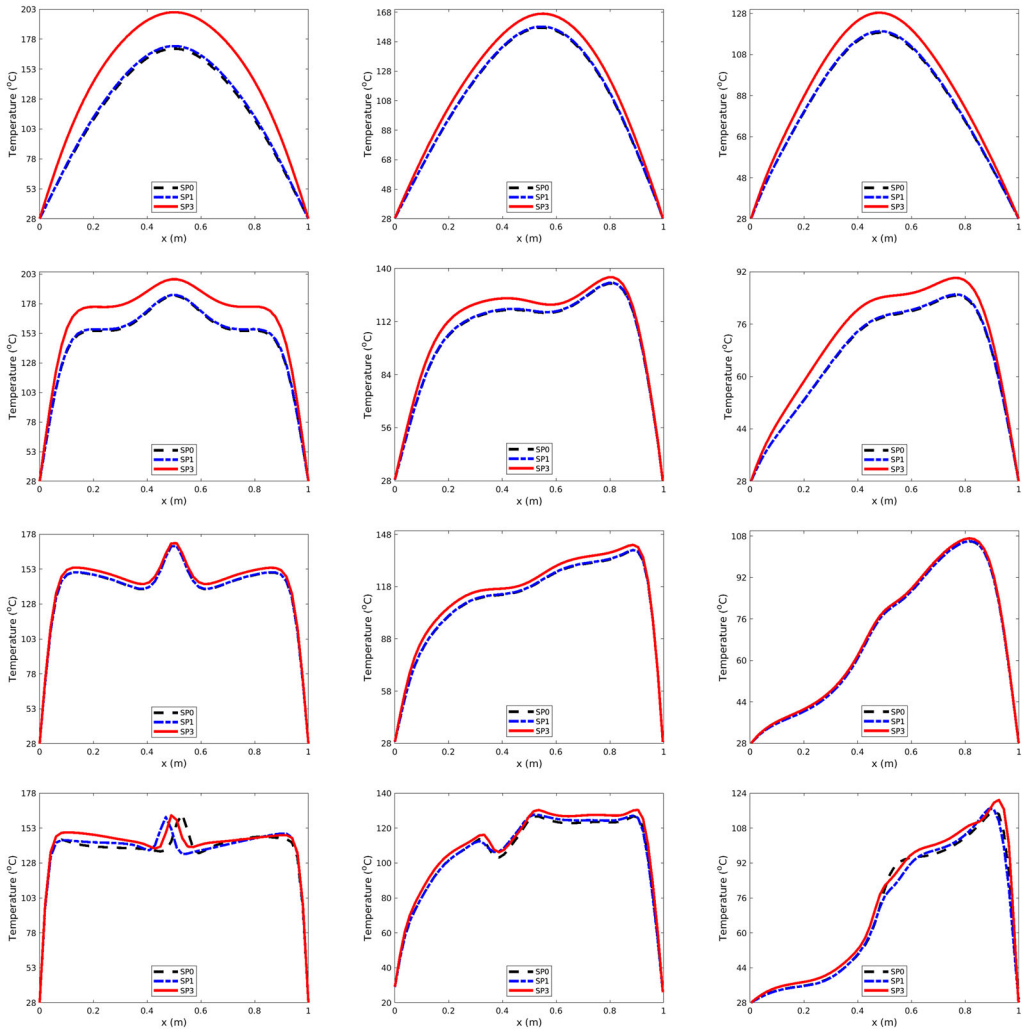


**Figure 21.** Temperature contour for the SP<sub>3</sub> solution at  $Ra = 10^4$  (first row),  $Ra = 10^5$  (second row),  $Ra = 10^6$  (third row), and  $Ra = 10^7$  (fourth row) with  $Pl = 0.2$  at  $\theta = 0^\circ$  (first column),  $\theta = 30^\circ$  (second column) and  $\theta = 60^\circ$  (third column).

flow recirculates anti clockwise. This is due to the buoyancy forces. Although the upper and lower surfaces are adiabatic, it should be noted that the temperature isotherms are not perpendicular to the adiabatic walls owing to the presence of the inclined angle, the radiation and convection heat transfer. The gradients of temperature increase at the top of the cavity as the hot air get less dense (lighter) when it is heated up. However, when the inclined angle increases the direction of the stagnant position gets affected by the buoyancy forces. It is worth mentioning that the recirculation of the flow covers the entire cavity and concentrated at the center of the cavity despite the value of the angle. As the cavity is inclined, the buoyancy driving force for the natural convection boundary layers will reduce, where the buoyancy term varies with  $\cos(\theta)$ . This kind of the buoyancy flow has been monitored at  $\theta = 0^\circ$  by [15]. The next step studies the effect of Planck constant. Figures 18 and 32 show the cross-sectional study for temperature at the center of the square cavity at the three mentioned angle for the considered Rayleigh numbers. At a  $Pl = 0.5$ , the ration of radiation to convection heat decreases, although this variation with optical depth remains the same. When Rayleigh number increases, the effect of radiation decreases dramatically even at a lower value of Planck constant. his indicates that when convection is more

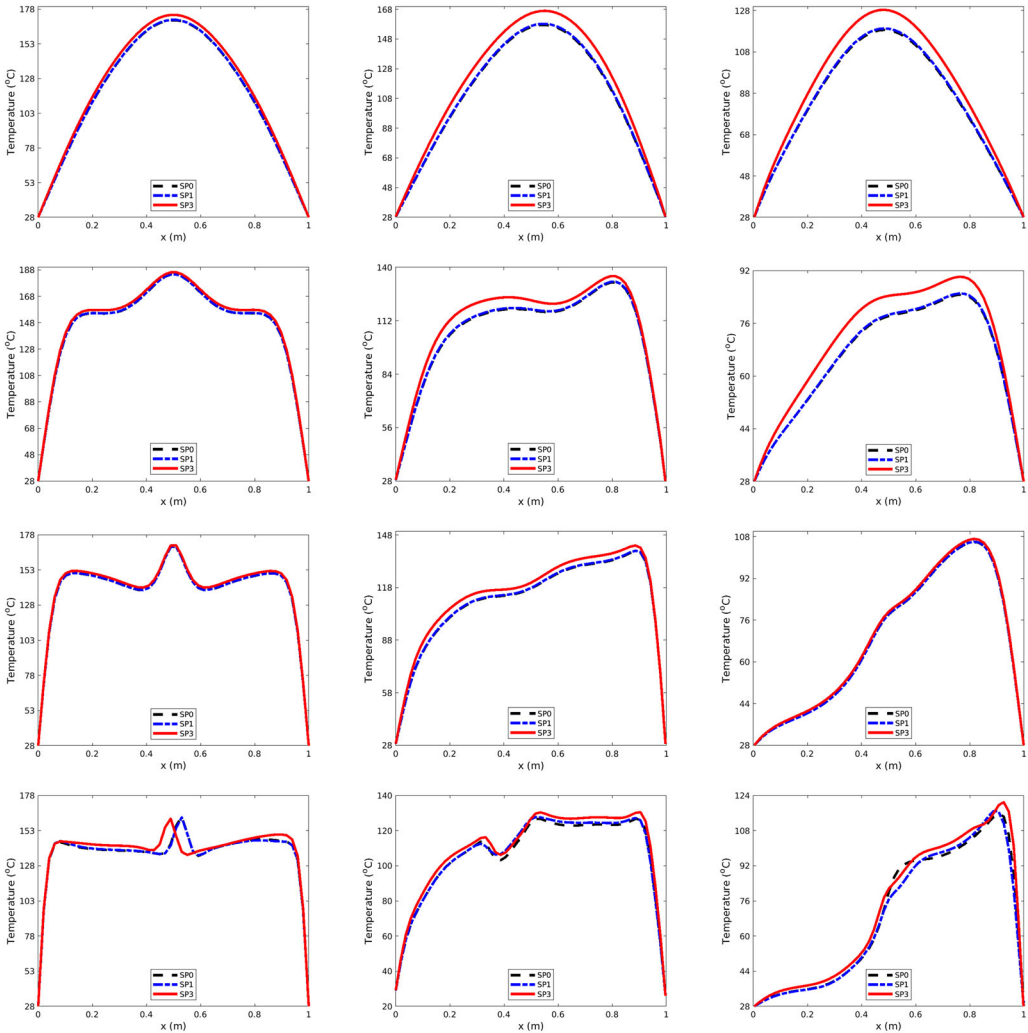


**Figure 22.** Temperature contour for the SP<sub>3</sub> solution at Ra = 10<sup>4</sup> (first row), Ra = 10<sup>5</sup> (second row), Ra = 10<sup>6</sup> (third row), and Ra = 10<sup>7</sup> (fourth row) with PI = 0.5 at θ = 0° (first column), θ = 30° (second column) and θ = 60° (third column).

**Table 1.** Temperature values in the middle of the geometry without including the circular heater in °C of SP<sub>0</sub>, SP<sub>1</sub>, and SP<sub>3</sub> at the chosen experimental simulations of θ = 0°.

Ra = 10 <sup>4</sup>					Ra = 10 <sup>5</sup>				
PI = 0.2			PI = 0.5		PI = 0.2			PI = 0.5	
SP <sub>0</sub>	SP <sub>1</sub>	SP <sub>3</sub>	SP <sub>1</sub>	SP <sub>3</sub>	SP <sub>0</sub>	SP <sub>1</sub>	SP <sub>3</sub>	SP <sub>1</sub>	SP <sub>3</sub>
128.14	132.38	154.63	130.17	139.89	127.85	130.48	143.27	129.44	137.24
Ra = 10 <sup>6</sup>					Ra = 10 <sup>7</sup>				
PI = 0.2			PI = 0.5		PI = 0.2			PI = 0.5	
SP <sub>0</sub>	SP <sub>1</sub>	SP <sub>3</sub>	SP <sub>1</sub>	SP <sub>3</sub>	SP <sub>0</sub>	SP <sub>1</sub>	SP <sub>3</sub>	SP <sub>1</sub>	SP <sub>3</sub>
127.95	129.47	137.82	128.76	134.72	128.54	128.95	134.84	128.93	133.17

intense, the effect of radiation gets smaller. For the case of PI = 0.2 in which the radiation is more dominant over the conduction, isotherms are high, unlike the pure convection condition where the heat did not reach the cold side, the adiabatic wall condition requires that the conductive heat equals to the radiative heat. If the latter is similar or larger than the former, there will be a temperature gradient near the wall. There are two evident changes to the temperature contour.

**Table 2.** Temperature values in the middle of the geometry without including the circular heater in °C of SP<sub>0</sub>, SP<sub>1</sub>, and SP<sub>3</sub> at the chosen experimental simulations of  $\theta = 30^\circ$ .

Ra = 10 <sup>4</sup>					Ra = 10 <sup>5</sup>				
PI = 0.2			PI = 0.5		PI = 0.2			PI = 0.5	
SP <sub>0</sub>	SP <sub>1</sub>	SP <sub>3</sub>	SP <sub>1</sub>	SP <sub>3</sub>	SP <sub>0</sub>	SP <sub>1</sub>	SP <sub>3</sub>	SP <sub>1</sub>	SP <sub>3</sub>
140.67	158.54	173.82	153.16	155.76	128.45	143.97	148.25	136.13	138.12
Ra = 10 <sup>6</sup>					Ra = 10 <sup>7</sup>				
PI = 0.2			PI = 0.5		PI = 0.2			PI = 0.5	
SP <sub>0</sub>	SP <sub>1</sub>	SP <sub>3</sub>	SP <sub>1</sub>	SP <sub>3</sub>	SP <sub>0</sub>	SP <sub>1</sub>	SP <sub>3</sub>	SP <sub>1</sub>	SP <sub>3</sub>
130.39	135.64	137.42	135.11	136.88	131.56	136.67	138.66	133.44	135.02

**Table 3.** Temperature values in the middle of the geometry without including the circular heater in °C of SP<sub>0</sub>, SP<sub>1</sub>, and SP<sub>3</sub> at the chosen experimental simulations of  $\theta = 60^\circ$ .

Ra = 10 <sup>4</sup>					Ra = 10 <sup>5</sup>				
PI = 0.2			PI = 0.5		PI = 0.2			PI = 0.5	
SP <sub>0</sub>	SP <sub>1</sub>	SP <sub>3</sub>	SP <sub>1</sub>	SP <sub>3</sub>	SP <sub>0</sub>	SP <sub>1</sub>	SP <sub>3</sub>	SP <sub>1</sub>	SP <sub>3</sub>
128.73	146.14	149.71	140.06	142.65	130.92	145.52	150.36	138.05	140.16
Ra = 10 <sup>6</sup>					Ra = 10 <sup>7</sup>				
PI = 0.2			PI = 0.5		PI = 0.2			PI = 0.5	
SP <sub>0</sub>	SP <sub>1</sub>	SP <sub>3</sub>	SP <sub>1</sub>	SP <sub>3</sub>	SP <sub>0</sub>	SP <sub>1</sub>	SP <sub>3</sub>	SP <sub>1</sub>	SP <sub>3</sub>
130	135.89	137.74	135.22	137.07	131.69	137.01	139.27	134.2	135.51

**Table 4.** Temperature values in the middle of the geometry with the inclusion the circular heater in °C of SP<sub>0</sub>, SP<sub>1</sub>, and SP<sub>3</sub> at the chosen experimental simulations of  $\theta = 0^\circ$ .

Ra = 10 <sup>4</sup>					Ra = 10 <sup>5</sup>				
PI = 0.2			PI = 0.5		PI = 0.2			PI = 0.5	
SP <sub>0</sub>	SP <sub>1</sub>	SP <sub>3</sub>	SP <sub>1</sub>	SP <sub>3</sub>	SP <sub>0</sub>	SP <sub>1</sub>	SP <sub>3</sub>	SP <sub>1</sub>	SP <sub>3</sub>
169.97	172.19	200.44	170.27	173.84	184.46	185.27	198.54	184.6	186.16
Ra = 10 <sup>6</sup>					Ra = 10 <sup>7</sup>				
PI = 0.2			PI = 0.5		PI = 0.2			PI = 0.5	
SP <sub>0</sub>	SP <sub>1</sub>	SP <sub>3</sub>	SP <sub>1</sub>	SP <sub>3</sub>	SP <sub>0</sub>	SP <sub>1</sub>	SP <sub>3</sub>	SP <sub>1</sub>	SP <sub>3</sub>
169.27	169.42	171.39	169.36	170.37	162.95	160.87	162.13	162.33	161.42

First, the temperature gradient reduced with the increase values of Planck constant which indicates more heat radiation intensity flows in a random directions and angles. Another difference is the isotherm is that skewness appears in the middle of the domain toward the hot wall side. For a value of PI = 0.5, isotherms have almost the same behavior at different values of optical depth. In this condition where the conduction heat transfer dominates over the radiation and the radiation is small compared with the diffusion heat. These results mean that the effect of heat in case of larger PI is only due to the adiabatic wall condition. Results show that the temperature layers are thinner than the case of Ra = 10<sup>4</sup>. As mentioned before, for a Planck constant PI = 0.5, the heat transfer acts somewhat same like the pure convection heat transfer as the convection heat becomes dominant. It can be seen that the heat flow decreases along the cold wall and tends to accumulate at the hot wall. The flow with an inclined angle has a dramatic effect on the heat flow behavior. The graph of isotherms shows a reduction in the transfer of heat as compared with the results conducted at  $\theta = 0^\circ$ . The flow of the temperature contour shows a reduction of almost 30% in the heat flow toward the cold direction. Heat is accumulating at the hot wall with reduction in the effect of heat radiation as compared with the results with the horizontal domain (without angle rotation). This unsteady flow is involved of a series of waves circulating around the edges of the cavity and traveling in the same direction as the flow, that is up the heated wall, from left to right across the cavity adjacent to the adiabatic walls. The transition flow is the result of both the natural convection boundary layers and the attached jet/plumes being able to sustain

traveling waves. Although the heat transfer is stable, at an inclination angle of  $30^\circ$  the desolation in the heat plumes is balanced by the expansion in the natural convection boundary layers which leads to the observed transition.

## 6.2. Cavity with internal complex geometry heater

The second part of the study has been considered for a square cavity with adiabatic upper and lower walls. The left and the right walls are kept at room temperature which is  $28^\circ\text{C}$ . A circular heater is installed at the center of the square cavity at a temperature of  $228^\circ\text{C}$ . Same heat transfer characteristics are taken into account in this second case study. Figure 20 shows the  $SP_3$  evolution of the thermal plume at the three mentioned angles. This evolution of the thermal plume can be defined as the interaction between the thermal plume at high temperature from the circular heating element and the thermal plume at lower temperature at the sides of the cavity. It can still be seen that the temperature distribution inside the cavity is affected by Rayleigh number and the inclined angle. At a dominant heat radiation ( $Ra = 10^4$ ), thermal plume tends to move upward. The only reason for this behavior is the presence of the adiabatic wall. However, at higher values of Rayleigh number, fluid flow rate increase and it is flowing toward the shortest cold region. This is due to the fact that the capability of the cold walls to absorb heat is more than the heat flux flow into the adiabatic upper wall at higher  $Ra$  and with the inclination of the angles. Since the temperature difference is established across the right side of the cavity, the gas starts to flow toward that direction and accumulates there. Figures 21 and 36 show the horizontal cross-sectional study that has been accounted across the cavity at  $y = 0.8$ . It can be seen that the effect of radiation is not quite dominant. Different values of Planck constant cannot increase the effect of radiation. This is due to the close distance of the heating element which is located in the middle. Introducing the heating element in the middle part of the cavity caused less heat transfer circulation across the geometry. This indicates that the longer the heat travels, the higher radiation of heat becomes. The effect of the adiabatic walls on the distribution of heat reduced massively with the augmentation of the inclined angle.

## 7. Concluding remarks

Combined heat transfer of natural convection and radiation in a 2D square cavity was studied numerically at three different inclined angles. The continuity, momentum and energy equations were solved using Taylor–Hood finite element approach. The medium was considered air with two upper and lower adiabatic walls. The heat transfer characteristics of the cavity were analyzed at a broad range of Rayleigh numbers ( $10^4$ – $10^7$ ) with optical thickness value of 0.1 and the Planck constant values of 0.2 and 0.5.

The complete study has been summarized in the Tables 1–4. It can be seen from the tables that the inclined cavity with angles of inclination of  $30^\circ$  and  $60^\circ$  is shown to have a considerably different flow effect to that of the noninclined cavity. The fluid in the diffuse intrusion travels horizontally across the cavity to be entrained by the far wall boundary layer. Furthermore, the average Nusselt number on the hot and cold walls is seen to be affected by the inclination angle. As the angle of inclination increases the fluid flow pattern changes. This change is due to the change in the buoyancy forces in the direction of flow between the hot and the cold walls. The effect of the inclusion of the heater element inside the square cavity gets effected mainly by the inclined angle then Rayleigh number.

## References

- [1] K. Lari, M. Baneshi, S. A. Gandjalikhan Nassab, A. Komiya, and S. Maruyama, “Combined heat transfer of radiation and natural convection in a square cavity containing participating gases,” *Int. J. Heat Mass Transfer.*, vol. 54, nos. 23–24, pp. 5087–5099, 2011. Copyright © 2011: International Journal of Heat and

- Mass Transfer, published by Elsevier Masson SAS. All rights reserved. DOI: [10.1016/j.ijheatmasstransfer.2011.07.026](https://doi.org/10.1016/j.ijheatmasstransfer.2011.07.026).
- [2] Y. Sun, X. Zhang, and J. Howell, "Assessment of different radiative transfer equation solvers for combined natural convection and radiation heat transfer problems," *J. Quant. Spectrosc. Radiat. Transfer.*, vol. 194, pp. 31–46, 2017. Copyright © 2017: J. Quant. Spectr. and Radiative Transfer, published by Elsevier Masson SAS. All rights reserved. DOI: [10.1016/j.jqsrt.2017.03.022](https://doi.org/10.1016/j.jqsrt.2017.03.022).
  - [3] G. Barakos, E. Mitsoulis, and D. Assimacopoulos, "Natural convection flow in a square cavity revisited: Laminar and turbulent models with wall functions," *Int. J. Numer. Meth. Fluids.*, vol. 18, no. 7, pp. 695–719, 1994. DOI: [10.1002/flid.1650180705](https://doi.org/10.1002/flid.1650180705).
  - [4] T. Fusegi, J. M. Hyun, K. Kuwaharas, and B. Farouk, "A numerical study of three-dimensional natural convection in a differentially heated cubical enclosure," *Int. J. Heat Mass Transf.*, vol. 34, no. 6, pp. 1543–1557, 1991. DOI: [10.1016/0017-9310\(91\)90295-P](https://doi.org/10.1016/0017-9310(91)90295-P).
  - [5] G. Lauriat, "Combined radiation–convection in gray fluids enclosed in vertical cavities," *Int. J. Heat Mass Transf.*, vol. 104, no. 4, pp. 609–615, 1982. DOI: [10.1115/1.3245175](https://doi.org/10.1115/1.3245175).
  - [6] G. Lauriat, "Numerical study of the interaction of natural convection with radiation in nongray gases in a narrow vertical cavity," *Int. J. Heat Mass Transf.*, vol. 2, pp. 153–158, 1982.
  - [7] A. Draoui, F. Allard, and C. Beghein, "Numerical analysis of heat transfer by natural convection and radiation in participating fluids enclosed in square cavities," *Numer. Heat Trans. A*, vol. 20, no. 2, pp. 253–261, 1991. DOI: [10.1080/10407789108944820](https://doi.org/10.1080/10407789108944820).
  - [8] S. K. Mahapatra, S. Sen, and A. Sarkar, "Interaction of surface radiation and variable property natural convection in a differentially heated square cavity—a finite element analysis," *Int. J. Numer. Methods Heat Fluid Flow*, vol. 9, no. 4, pp. 423–443, 1999. DOI: [10.1108/09615539910266594](https://doi.org/10.1108/09615539910266594).
  - [9] H. Bouali, A. Mezrhab, H. Amaoui, and M. Bouzidi, "Radiation–natural convection heat transfer in an inclined rectangular enclosure," *Int. J. Therm. Sci.*, vol. 45, no. 6, pp. 553–566, 2006. DOI: [10.1016/j.ijthermalsci.2005.10.001](https://doi.org/10.1016/j.ijthermalsci.2005.10.001).
  - [10] Z. Tan and J. Howel, "Combined radiation and natural convection in a two-dimensional participating square medium," *Int. J. Therm. Sci.*, vol. 34, no. 3, pp. 785–793, 1991. DOI: [10.1016/0017-9310\(91\)90125-X](https://doi.org/10.1016/0017-9310(91)90125-X).
  - [11] V. Vivek, A. Sharma, and C. Balaji, "Interaction effects between laminar natural convection and surface radiation in tilted square and shallow enclosures," *Int. J. Therm. Sci.*, vol. 60, pp. 70–84, 2012. DOI: [10.1016/j.ijthermalsci.2012.04.021](https://doi.org/10.1016/j.ijthermalsci.2012.04.021).
  - [12] P. Kumar and V. Eswaran, "The effect of radiation on natural convection in slanted cavities of angle  $\gamma = 45^\circ$  and  $60^\circ$ ," *Int. J. Therm. Sci.*, vol. 67, pp. 96–106, 2013. DOI: [10.1016/j.ijthermalsci.2012.12.009](https://doi.org/10.1016/j.ijthermalsci.2012.12.009).
  - [13] M. Leporini, F. Corvaro, B. Marchetti, F. Polonara, and M. Benucci, "Experimental and numerical investigation of natural convection in tilted square cavity filled with air," *Exp. Therm. Fluid Sci.*, vol. 99, pp. 572–583, 2018. DOI: [10.1016/j.expthermflusci.2018.08.023](https://doi.org/10.1016/j.expthermflusci.2018.08.023).
  - [14] J. Wang, M. Yang, and Y. Zhang, "Onset of double-diffusive convection in horizontal cavity with Soret and Dufour effects," *Int. J. Heat Mass Transf.*, vol. 78, pp. 1023–1031, 2014. DOI: [10.1016/j.ijheatmasstransfer.2014.07.064](https://doi.org/10.1016/j.ijheatmasstransfer.2014.07.064).
  - [15] M. Nia and S. Nassab, "Thermohydrodynamic characteristics of combined double-diffusive radiation convection heat transfer in a cavity," *Comptes Rendus Mecanique*, vol. 347, pp. 406–422, 2019. Copyright © 2019: Comptes Rendus Mecanique, published by Elsevier Masson SAS. All rights reserved.
  - [16] S. Mikhailenko, M. Sheremet, and A. Mohamad, "Convective-radiative heat transfer in a rotating square cavity with a local heat-generating source," *Int. J. Mech. Sci.*, vols. 142–143, pp. 530–540, 2018. DOI: [10.1016/j.ijmecsci.2018.05.030](https://doi.org/10.1016/j.ijmecsci.2018.05.030).
  - [17] G. Kefayati, "Double-diffusive natural convection and entropy generation of Bingham fluid in an inclined cavity," *Int. J. Heat Mass Trans.*, vol. 116, pp. 762–812, 2018. Copyright © 2018: International Journal of Heat and Mass Transfer, published by Elsevier Masson SAS. All rights reserved. DOI: [10.1016/j.ijheatmasstransfer.2017.09.065](https://doi.org/10.1016/j.ijheatmasstransfer.2017.09.065).
  - [18] Y. Jaluria, *Natural Convection Heat and Mass Transfer*. Oxford: Pergamon Press, 1980.
  - [19] M. F. Modest, *Radiative Heat Transfer*. New York: McGraw-Hill, 1993.
  - [20] E. Larsen, G. Thömmes, A. Klar, M. Seaid, and T. Götz, "Simplified  $P_N$  approximations to the equations of radiative heat transfer and applications," *J. Comp. Phys.*, vol. 183, no. 2, pp. 652–675, 2002. DOI: [10.1006/jcph.2002.7210](https://doi.org/10.1006/jcph.2002.7210).
  - [21] M. El-Amrani and M. Seaid, "Numerical simulation of natural and mixed convection flows by Galerkin-characteristic method," *Int. J. Num. Meth. Fluids*, vol. 53, no. 12, pp. 1819–1845, 2006, to appear.
  - [22] J. Douglas and T. F. Russell, "Numerical methods for convection dominated diffusion problems based on combining the method of characteristics with finite elements or finite differences," *SIAM J. Numer. Anal.*, vol. 19, no. 5, pp. 871–885, 1982. DOI: [10.1137/0719063](https://doi.org/10.1137/0719063).
  - [23] O. Pironneau, "On the transport-diffusion algorithm and its applications to the Navier–Stokes equations," *Numer. Math.*, vol. 38, no. 3, pp. 309–332, 1982. DOI: [10.1007/BF01396435](https://doi.org/10.1007/BF01396435).

- [24] E. Sili, "Convergence and nonlinear stability of the Lagrange–Galerkin method for the Navier–Stokes equations," *Numer. Math.*, vol. 53, pp. 459–483, 1988.
- [25] C. Temperton and A. Staniforth, "An efficient two-time-level semi-Lagrangian semi-implicit integration scheme," *QJR Meteorol. Soc.*, vol. 113, no. 477, pp. 1025–1039, 1987. DOI: [10.1002/qj.49711347714](https://doi.org/10.1002/qj.49711347714).
- [26] M. Seaïd, "Semi-Lagrangian integration schemes for viscous incompressible flows," *Comput. Methods Appl. Math.*, vol. 2, no. 4, pp. 392–409, 2002. DOI: [10.2478/cmam-2002-0022](https://doi.org/10.2478/cmam-2002-0022).
- [27] M. Seaïd and M. El-Amrani, "Lagrange–Galerkin method for unsteady free surface water waves," *Comput. Visual. Sci.*, vol. 9, no. 4, pp. 209–228, 2006, in press. DOI: [10.1007/s00791-006-0027-8](https://doi.org/10.1007/s00791-006-0027-8).
- [28] M. Bercovier and O. Pironneau, "Error estimates for finite element solution of the Stokes problem in the primitive variables," *Numer. Math.*, vol. 33, no. 2, pp. 211–224, 1979. DOI: [10.1007/BF01399555](https://doi.org/10.1007/BF01399555).
- [29] R. Verfürth, "Error estimates for a mixed finite element approximation of the Stokes equation," *RAIRO. Anal. Numér.*, vol. 18, no. 2, pp. 175–182, 1984. DOI: [10.1051/m2an/1984180201751](https://doi.org/10.1051/m2an/1984180201751).
- [30] C. Johnson, *Numerical Solution of Partial Differential Equations by the Finite Element Method*. Cambridge University Press: Cambridge-Lund, 1987.
- [31] S. M. Bajorek and J. R. Lloyd, "Experimental investigations of natural convection in partitioned enclosures," *ASME J. Heat Transf.*, vol. 104, no. 3, pp. 527–532, 1982. DOI: [10.1115/1.3245125](https://doi.org/10.1115/1.3245125).
- [32] R. A. Kuyper, T. Van Der Meer, C. J. Hoogendoorn, and R. Henkes, "Numerical study of laminar and turbulent natural convection in an inclined square cavity," *Int. J. Heat Mass Transf.*, vol. 36, no. 11, pp. 2899–2911, 1993. Copyright © 1993: International Journal of Heat and Mass transfer, published by Elsevier Masson SAS. All rights reserved. DOI: [10.1016/0017-9310\(93\)90109-J](https://doi.org/10.1016/0017-9310(93)90109-J).
- [33] S. Acharya, "Natural convection in an inclined enclosure containing internal energy sources and cooled from below," *Int. J. Heat Fluid Flow*, vol. 6, no. 2, pp. 113–121, 1985. Copyright © 1985: International Journal of Heat & Fluid Flow, published by Elsevier Masson SAS. All rights reserved. DOI: [10.1016/0142-727X\(85\)90045-1](https://doi.org/10.1016/0142-727X(85)90045-1).
- [34] H. Park, M. Ha, H. Yoon, Y. Park, and C. Son, "A numerical study on natural convection in an inclined square enclosure with a circular cylinder," *Int. J. Heat Mass Transf.*, vol. 66, pp. 295–314, 2013. Copyright © 2013: International Journal of Heat and Mass transfer, published by Elsevier Masson SAS. All rights reserved. DOI: [10.1016/j.ijheatmasstransfer.2013.07.029](https://doi.org/10.1016/j.ijheatmasstransfer.2013.07.029).
- [35] T. H. Kuehn and R. J. Goldstein, "An experimental and theoretical study of natural convection in the annulus between horizontal concentric cylinders," *J. Fluid Mech.*, vol. 74, no. 4, pp. 695–719, 1976. Copyright © 1976: Journal of Fluid Mechanics, published by Elsevier Masson SAS. All rights reserved. DOI: [10.1017/S0022112076002012](https://doi.org/10.1017/S0022112076002012).
- [36] X. Yang and S. C. Kong, "Numerical study of natural convection in a horizontal concentric annulus using smoothed particle hydrodynamics," *Eng. Anal. Bound. Elem.*, vol. 102, pp. 11–20, 2019. Copyright © 2019: Engineering Analysis with Boundary Elements, published by Elsevier Masson SAS. All rights reserved. DOI: [10.1016/j.enganabound.2019.02.007](https://doi.org/10.1016/j.enganabound.2019.02.007).
- [37] X. Yuan, F. Tavakkoli, and K. Vafai, "Analysis of natural convection in horizontal concentric annuli of varying inner shape," *Numer. Heat Transf.*, vol. 68, no. 11, pp. 1155–1174, 2015. DOI: [10.1080/10407782.2015.1032016](https://doi.org/10.1080/10407782.2015.1032016).
- [38] B. Jha, I. Yabo, and J. E. Lin, "Transient natural convection in an annulus with thermal radiation," *AM*, vol. 08, no. 09, pp. 1351–1366, 2017. DOI: [10.4236/am.2017.89100](https://doi.org/10.4236/am.2017.89100).
- [39] M. Sheikholeslami, M. Gorji-Bandpy, D. Ganji, and S. Soleimani, "Effect of a magnetic field on natural convection in an inclined half-annulus enclosure filled with Cu-water nanofluid using CVFEM," *Adv. Powder Technol.*, vol. 24, no. 6, pp. 980–991, 2013. Copyright © 2013: Advanced Power Technology, published by Elsevier Masson SAS. All rights reserved. DOI: [10.1016/j.apt.2013.01.012](https://doi.org/10.1016/j.apt.2013.01.012).
- [40] K. Liou, "An introduction to atmospheric radiation," *Int. Geophys.*, vol. 84, pp. 1–583, 2002.